Vehicular Communications 46 (2024) 100730

Contents lists available at ScienceDirect

Vehicular Communications

journal homepage: www.elsevier.com/locate/vehcom

Energy-minimizing 3D circular trajectory optimization of rotary-wing UAV under probabilistic path-loss in constrained hotspot environments

Enzo Baccarelli, Michele Scarpiniti *, Alireza Momenzadeh

Department of Information Engineering, Electronics and Telecommunications (DIET), Sapienza University of Rome, Via Eudossiana 18, 00184 Rome, Italy

ARTICLE INFO

Keywords:
Rotary-wing UAV
QoS-constrained aerial coverage
Adaptive trajectory optimization
SDN/NFV-based UAV architectures
UAV-supported microservice orchestration

ABSTRACT

In this paper, we consider a Software Defined Networking (SDN)/Network Function Virtualized (NFV) networked computing system, which is composed of a serving Rotary Wing (RW) Unmanned Aerial Vehicle (UAV), a Ground Controller Station (GCS) and a number of resource-limited (possibly, heterogeneous) Ground Users (GUs) that randomly move in environments affected by fading-induced probabilistic path-loss. The focus of this paper is on the joint and adaptive optimization of the 3D trajectory parameters (i.e., altitude, radius, and speed) of the RW-UAV that circulates over the served hotspot area for providing communication and/or computing support to the GUs. The objective is the minimization of the RW-UAV propulsion energy under constraints on the maximum allowed average path-loss, maximum tolerated outage probability, and finite beam-width of the UAV antenna. Due to the acceleration-dependent terms present in the considered RW-UAV energy propulsion model, the formulated problem is non-convex, and up to now, its solution still appears not to be addressed in the literature. Hence, to tackle this challenging problem: 1) we develop a (seemingly new) convexification approach to turn the problem into a Geometric Programming (GP) one; 2) after characterizing the related feasibility conditions, we develop an adaptive solving approach that relies on primal-dual gradient-based iterations; and, then, 3) we perform a joint co-design of the main blocks of the SDN/NFV-based communication/computing architectures equipping the serving RW-UAV and controlling GCS, in order to provide support for the orchestration of the computing/communication microservices possibly required by the served GUs. The conducted numerical tests confirm that the performance gains of the proposed optimization framework against the ones of a number of baselines may reach 22%, while the corresponding performance gaps against the ultimate performance of a brute force search-based benchmark remain typically limited up to 3%-4%.

1. Motivations and goals

Using Unmanned Aerial Vehicles (UAVs), e.g. drones, as flying base stations, access points and/or computing (e.g. Fog) nodes for providing temporary aerial coverage to communication and/or computing resource-limited Ground Users (GUs) in hotspot applications is considered a main target of the sixth generation (6G) wireless network paradigm [1,2]. The peculiar UAV capability of adjusting its spatial (i.e., 3D) mobile trajectory allows to increase the probability of Line-of-Sight terrestrial-air links. This opens the doors to the feasibility of dynamic provisioning of UAV-based temporary communication/computing support in hotspot areas or terrestrial infrastructure-less environments, like [3–5]: (i) disaster areas affected by (temporary) unavailability of terrestrial infrastructure; (ii) social events, in which terrestrial communication infrastructure (if present) is temporarily overloaded; and, (iii) hotspot areas in vehicular communication scenarios. Preliminary insight about the practical feasibility of these cases of UAV use has been provided, for instance, by the European ABSOLUTE project [6].

In principle, terrestrial WiFi offloading and/or pico-cells are capable of managing hotspot events, but their deployments require to install fixed terrestrial access points and/or small terrestrial base stations [4,7]. In hotspot scenarios, UAV-supported data/computation offloading would represent a more cost-effective solution due to the less energy-supplies/aircraft costs [1,8]. However, due to the limited on-board energy, UAV spatial deployment and trajectory planning should be so designed that the resulting UAV energy consumption is minimized under constraints on the wireless coverage and GU service demands [5,8].

* Corresponding author.
E-mail addresses: enzo.baccarelli@uniroma1.it (E. Baccarelli), michele.scarpiniti@uniroma1.it (M. Scarpiniti), alireza.momenzadeh@uniroma1.it (A. Momenzadeh).

https://doi.org/10.1016/j.vehcom.2024.100730
Received 16 May 2023; Received in revised form 2 October 2023; Accepted 19 January 2024
Available online 24 January 2024

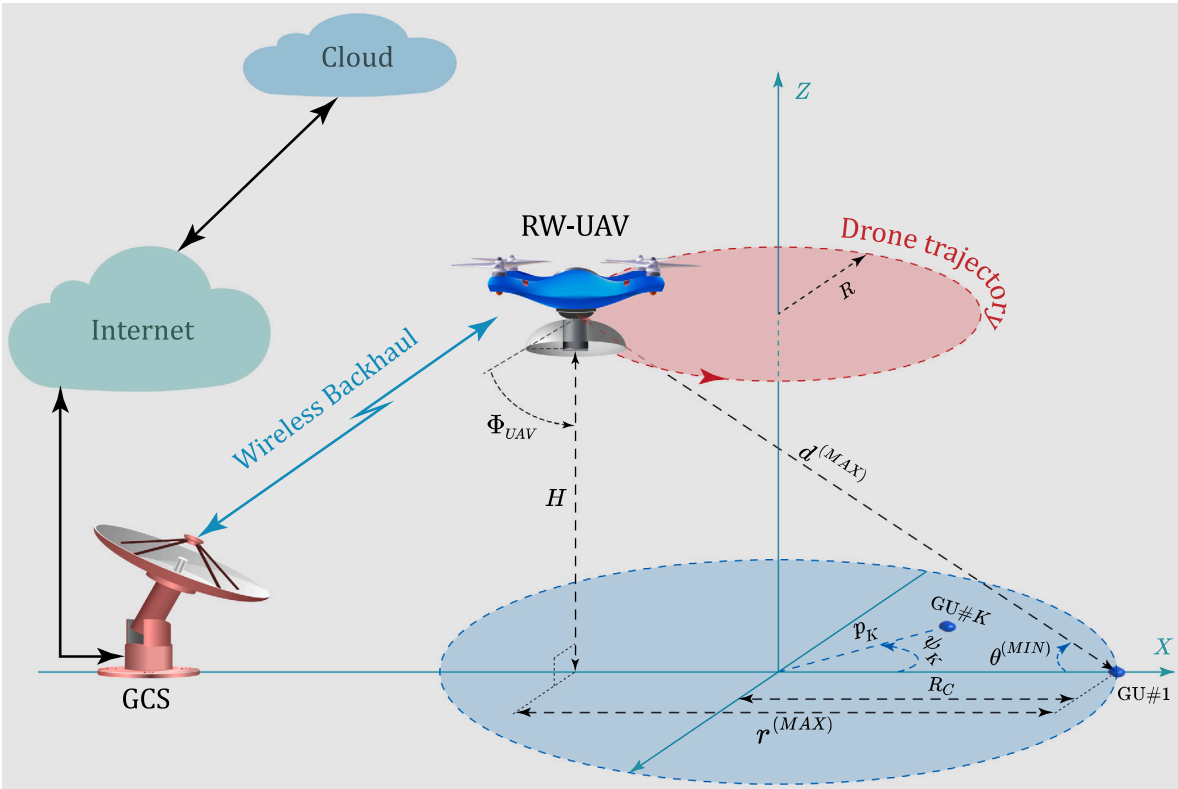

Fig. 1. A sketch of the considered UAV-supported hotspot scenario. RW: = Rotary-Wing; GCS: = Ground Control Station.

1.1. Considered application scenario and paper's focus

Motivated by these considerations, we consider the hotspot application scenario of Fig. 1.

In this scenario, a (possibly, time-variant and 'a priori' unknown) number of (possibly, heterogeneous) GUs is deployed over a disk-shaped coverage area. GUs could randomly (and even unpredictably) move over ground trajectories [9]. The goal of the RW-UAV is to provide wireless coverage [4] and possibly computing support to the GUs [5]. For this reason, the RW-UAV of Fig. 1 cyclically flies along a circular trajectory, whose altitude, radius, and speed are fixed but adjustable. Each terrestrial-aerial GU-UAV link is affected by random blocking phenomena, so that it randomly alternates Line-of-Sight (LoS) and Non-Line-of-Sight ($NLoS$) states according to a given LoS probability model. Furthermore, depending on the actual system deployment, the UAV operations may be controlled by a Ground Control Station (GCS). When the GCS is present, the UAV-GCS backhaul path can be implemented via out-of-band radio or Free Space Optical (FSO)-based high-capacity links (see Fig. 1), which may be established and managed without involving the GUs [10].

We point out that, in the reference framework of Fig. 1:

(i) the involved GUs may be heterogeneous in terms of transmit powers, demanded (e.g., target) communication bit rates, required communication bandwidths, experienced noise and/or multiple-access interference power levels (see Section 6.1);
(ii) the network topology of Fig. 1 is of star type, with the RW-UAV acting as central node. This means that, in Fig. 1: (a) GU-to-GU communications exploit the RW-UAV as switch node; while, (b) each GU may access the remote Internet by using the RW-UAV and GCS as network gateways (see Section 6.2); and,
(iii) network stability is enforced by limiting the worst-case average path-loss suffered by each GU-UAV up/down-link up to a finite threshold: TH_{PL}, which, in turn, depends on the set of the average target bit-rates demanded by the GUs (see Eqs. (19) and (50)).

Paper's focus Although RW-UAVs may be held aloft, nevertheless, hovering in the sky is not energy efficient [11,12]. Hence, in this paper, we consider the constrained minimization of the RW-UAV propulsion energy via the joint optimization of the altitude, radius, and period of the followed circular trajectory.[1] The considered constraints include: (i) the minimum and maximum values allowed the optimized variables; (ii) the upper bound on the coverage radius dictated by the finite beam-width of the UAV antenna; (iii) the upper bound on the (GU position-depending and time-varying) average path losses experienced by the GU-UAV up/down links of Fig. 1; and, (iv) the upper-bound on the (QoS-dictated) per-GU out-of-service probability. The novelty of the afforded problem is that, since the considered circular trajectory is required to explicitly take the UAV centrifugal acceleration into account, we must resort to the acceleration-dependent model for the RW-UAV propulsion power, recently presented in [13]. In this regard, we note that, on the basis of the overview of the related work given in Section 2, up until now, acceleration-dependent propulsion models for RW-UAVs still seem not to be employed in solving trajectory optimization problems under path-loss constrains and/or QoS-dictated constraints on the desired target in-service probability. In particular, to the best of the authors' knowledge, we point out that until now, studies on the 3D spatial placement and 3D trajectory optimization of RW-UAVs rely on the acceleration-independent propulsion power model presented in [11], which, from a formal point of view, applies only to constant-speed and straight (i.e. uniform and rectilinear) UAV trajectories.

1.2. Solving challenges, main contributions, and paper's roadmap

The afforded optimization problem is non-convex, mainly because: (i) the adopted propulsion model in [13] introduces *new* non-convex terms in the considered objective function; and (ii) in our framework, the resulting per-GU path loss function is the *non-convex* product of

[1] Or equivalently the angular speed of the circular trajectory.

two *non-convex* component functions that depend on the ('a priori' unknown) UAV-GU relative positions. As a consequence, the state-of-the-art solving approaches for the 2D/3D trajectory optimization of FW-UAVs or straight-flying RW-UAVs fall short of our framework.

Hence, the *main* contribution of our paper relies on the development of a (seemingly new) approach for the *joint* convexification of the propulsion power model in [13,14] *and* the per-GU path-loss functions. This is accomplished by introducing: (i) a set of suitable slack variables, which allow the uncoupling of some mixed speed and acceleration-dependent nonconvex terms; as well as (ii) a Quality-of-Service (*QoS*)-dictated constraint on the per-GU maximum allowed outage probability. The main features of the developed solving approach are that: (i) the proposed convexification procedure applies to every elevation angle-depending strictly-increasing LoS probability function; and (ii) the resulting convexified problem is an instance of Geometric Programming (GP), so that its *global optimal* solution can be numerically evaluated *without* using (cumbersome) Successive Convex-Approximation (SCA)-based approaches [10,14].

Besides these main contributions, *further* paper's contributions are that:

- we develop *closed-form* necessary and sufficient conditions for the feasibility of the GP problem. These allow to gain insight into the impact of the main system parameters on the ultimate system performance;
- we design a (seemingly new) regularized formula for the step-size updating, which exploits the available gradients for achieving adaptation to guarantee *fast* and *smooth enough* convergence in the presence of abrupt gradient changes; and,
- we provide a high-level *joint co-design* of the supporting communication/computing architectures of the serving UAV and GCS of Fig. 1. The co-design is carried out according to the emerging SDN/NFV virtualization paradigm. Its final goal is to allow the serving UAV to support the orchestration of the virtualized computing/communication services, possibly required by the GUs.

The performance sensitivity of the developed optimization framework is numerically checked under a number of $LoS/NLoS$ application environments, LoS probability models, and settings of the tolerated outage probability. The resulting performance comparison with some state-of-the-art baselines leads to the following three main conclusions. First, the energy reductions of the proposed joint optimization approach compared to some baselines that optimize only a subset of the UAV trajectory parameters may reach 22%. Second, the corresponding suffered energy gap compared to the ultimate performance of a brute force search-based benchmark that does *not* guarantee QoS maintains limited up to 3% - 4%. Third, the energy saving compared to a companion optimized system that utilizes a small size Fixed-Wing UAV (FW-UAV) for providing wireless coverage is beyond 12% and it can reach 30% under some specific operating environments.

Paper roadmap and adopted notation The rest of the paper is organized as follows. After the review on the related work of Section 2 and the system modeling of Section 3, the optimization problem is formalized in Section 4, while the developed solving approach is detailed in Section 5. After the presentation of the designed SDN/NFV-based orchestrating architecture of Section 6, in Section 7 we numerically test and compare the energy performance of the proposed optimization framework. Some remarks and hints for future research are provided in Section 8. Appendix A recaps the main adopted taxonomy and simulated setting, while Appendix B, Appendix C, and Appendix D report the proofs of some more formal results.

Regarding the main adopted notation, we point out that $\triangleq$ mean "equal by definition", symbols: $\vec{x}$, $\vec{Y}$ indicate 2D column vectors, where $x \triangleq \| \vec{x} \|$, $Y \triangleq \left\| \vec{Y} \right\|$ denote their Euclidean norms. Furthermore, $\square^T$ indicates vector transposition, while non-arrowed lower/upper italic letters: R, r denote scalar parameters.

2. Related work

In the recent years, mobile networked computing architectures that integrate ground and flying vehicles have been proposed as an effective means to provide wireless communication and computing support at the network edge in (typically, resource-constrained and energy-limited) infrastructure-less hotspot scenarios. The surveys in [15,16] overview the state-of-the-art, and discuss still open challenges concerning QoS wireless coverage, data offloading and Fog computing. The main focus of the tutorial in [17,18] is on the description of SDN/NFV-supported networked computing architectures for the UAV-aided delivering of heterogeneous services in multi-tenant (possibly, vehicular) environments. A number of topics related to the efficient energy-management of the resulting UAV-supported vehicular architectures has been recently discussed in [2].

On the basis of these (broad-spectrum) surveys, the research on the topics mostly related to the presented results here can be classified under five headings.

1. *1D UAV deployment under probabilistic link models* – The focus of the first set of papers is the 1D optimization of the UAV altitude to provide optimal ground coverage under fading-affected terrestrial-aerial links. In this regard, the (pioneering) contribution in [19] develops, and uses an analytical LoS probability model (the so called logistic LoS probability model) to optimize the altitude of a serving UAV. Afterwards, by using this model, the authors of [20] develop an algorithmic framework for optimizing the altitude of a drone small cell to maximize the terrestrial coverage, while minimizing the required communication power under both interference-affected and interference-free reference scenarios. The authors of [21] present a generalization of the original logistic LoS probability model (the so called generalized logistic LoS probability model) and use it to optimize both scheduling and transmit powers of the served ground sensors in urban environments. Like our contribution, all these works perform the optimization of the UAV altitude, but unlike our proposal, they *do not* consider the propulsion energy wasted by the serving UAV.

2. *2D UAV trajectory optimization under non-probabilistic link models* – The second set of contributions focuses on the optimized 2D deployment of (possibly, multiple) serving UAVs in the horizontal space. This set of papers *does not* optimize the UAV altitude and utilize the deterministic free-space formula for characterizing the gains of the involved aerial-terrestrial links. The other common feature of the papers in [22–25] is to consider *fixed-wing* UAVs that fly along *circular* trajectories. Specifically, in [22] the authors optimize the radius and speed of the circular FW-UAV trajectory, in order to maximize the resulting energy efficiency by taking into accounting the UAV propulsion energy. The results of the analysis, carried out in [22], are refined in [25], where the trade-off between communication energy of the served GUs and propulsion energy of the serving FW-UAV is further investigated. The proposal in [24] investigates the optimal communication strategy of a circulating FW-UAV that acts as aerial relay between two GUs. In particular, in [24], a variable-rate decode-and-forward relay protocol is designed and numerically validated, in order to maximize the resulting end-to-end data rate. Lastly, the goal of the work in [23] is the development of a dynamic UAV placement and radius adjustment algorithm for increasing the probability of link connections between a serving circulating FW-UAV and the served GUs. Overall, like our proposal, all these contributions consider circular trajectory as an effective way to provide aerial coverage to GUs with unknown (time-varying) positions. However, unlike our proposal, these works rely on non-probabilistic (fading-free) link models and the results of their analysis only apply to fixed-wing UAVs. Finally, like our contribution, in [14] the authors afford the topic of the trajectory optimization of a RW-UAV for maximizing the resulting energy efficiency by explicitly cosidering the RW-UAV propulsion

energy consumption. However, unlike our proposal, the work in [14]: (i) still assumes a fading-free scenario and characterizes the GU-UAV link gains through the free-space gain formula; (ii) does not optimize the UAV altitude; (iii) assumes that both the number of served GUs and their 2D locations are fixed and 'a priori' known; (iv) does not consider the coverage constraints induced by the beam-width of the UAV antenna; and finally, (v) does not enforce constraints on the desired target in-service probability. Similar conclusions hold for the analysis conducted in [11].

3. *3D UAV trajectory/deployment optimization under probabilistic/non-probabilistic link models* – After recognizing that the performance of UAV-assisted communication systems may significantly depend on both the UAV altitude and 2D UAV position, a third set of contributions focuses on the 3D trajectory/deployment optimization of (multiple) serving UAVs. To address this problem in hotspot scenarios, the general approach is to decouple the overall 3D optimization problem into two related sub-problems, which separately involve the vertical and planar coordinates [2]. In this regard, the goal of the contribution in [26] is the 3D placement of a single serving UAV in a hotspot area to maximize the covered area under probabilistic path loss. The authors of [27] develop a density-aware UAV placement algorithm, whose target is the maximization of the number of the served GUs under suitable QoS-enforced constraints. The proposal in [28] aims to deploy a Non Orthogonal Multiple Access (NOMA)-based HetNet supported by multiple UAVs, whose target is the joint minimization of the maximum UAV hovering time and the GU-to-GU communication power consumption. The goal of the contribution in [29] is to optimize the 3D placement of a serving UAV under in-band full-duplex communication to maximize the aggregated network throughput of the underlying HetNet. The study in [30] pursues the maximization of the per-GU minimum communication rate by jointly optimizing the 3D trajectories of the serving UAVs, GU scheduling, and GU-to-UAV association. Finally, the authors of [31] tackle the study of multi-drone-cell 3D trajectory design and GU scheduling to minimize the average per-GU path loss in UAV-assisted radio access networks for IoT data-gathering applications.

Like our contribution, the common feature of these papers is the optimization of the spatial trajectories of serving UAVs under a number of path-loss and/or QoS-dictated constraints. However, unlike our contribution, their focus is *not* the minimization of the propulsion energy of the serving UAVs.

4. *UAV support for Fog computing* – The main goal of state-of-the-art terrestrial Fog infrastructures is to shift computing resources to the network edge to provide computing support to resource-limited GUs [32]. However, it has been recently recognized that the use of UAVs as Fog servers enables also resource mobility, because such types of "flying" nodes can be quickly deployed and scaled up/down on demand [4]. This is the common scenario considered, for example, in [33–39], where RW-UAVs are used as Fog nodes as in Fig. 1. In this regard, the contributions in [33–35] focus on the optimized deployment of UAV-mounted Fog nodes, while trajectory optimization aspects are provided in [36–39]. The authors of [34] address the topic of the optimized deployment of UAV-mounted Fog nodes. Their goal is to efficiently manage the spatial and time fluctuations of the GU demands to maximize the number of processed requests and per-GU average service rates, while minimizing the number of deployed UAVs. For this reason, after formulating the afforded problem as a multi-objective integer linear problem, an iterative greedy-type heuristic is proposed as approximated solution and its performance is numerically tested. Hence, as in our contribution, the general problem of the optimal UAV coverage is afforded in [34]. However, unlike our contribution, in [34], the serving RW-UAVs are assumed to statically hover in the air, which is energy inefficient. The problem of the placement of UAV-mounted Fog servers is addressed in [11,35], with the goal of minimizing the per-GU access delay. This contribution shows that the volume of the aggregate offloaded data may increase compared to the case terrestrial Fog infrastructures, but the carried out analysis does not account for the energy consumption of the serving UAVs. The contribution in [33] considers an urban vehicular application scenario, in which UAV-mounted Fog nodes are dynamically dispatched during hotspot events to temporarily augment the computing capacity of the available terrestrial road side units. Although the authors of [33] formally prove that their proposed dispatching solution can reduce the service time of the offloaded tasks in path-loss affected urban environments, nevertheless, the conducted analysis does not consider the optimization of the UAV trajectory parameters, while the evaluation of the wasted propulsion energy relies on the acceleration-*independent* model of [11].

Concerning trajectory optimization aspects, the authors of [36] prove that the suitable optimization of the trajectories followed by UAV-mounted Fog servers can help the served GUs to save their communication energy. However, the analysis in [36] does not consider the corresponding energy consumption of the serving UAVs. In [37], this item is taken into account, where the UAV trajectory is so planned that jointly minimize the energy consumption of the served GUs and serving UAVs. The focus of the analysis in [38] is the energy consumption of the serving UAV and estimation of the GU positions, while the goal is the optimization of UAV trajectory. Finally, the authors of [39] introduce the additional ingredient of GU fairness in the formulation of the considered optimization problem and develop (heuristic) algorithms for the joint optimization of the UAV trajectory, GU scheduling, and allocation of the computing resources under inter-GU fairness constraints. Overall, like our contribution, all the papers [36–39] consider the optimization of the trajectories of RW UAV-mounted Fog servers under various system constraints. However, unlike our contribution, these works do *not* consider the related propulsion energy aspects, or rely on the acceleration-*independent* propulsion energy model of [11].

5. *NFV/SDN virtualization of UAV-supported networked computing architectures* – According to the 6G vision [1], [3], UAV-supported networks should be re-usable for heterogeneous missions. SDN and NFV enable fast on-demand reconfiguration of the underlying physical infrastructure by moving the programming of network and compute devices to a logically centralized controller, i.e. the GCS of Fig. 1. In principle, the main benefits, derived from uncoupling the control and data planes, embrace [40,18]: (i) the deployment of centralized resource orchestrators, which can be global and flexible; (ii) the development of on-demand resource allocation strategies that take the current link states and GU requirements into account; (iii) the virtualization of the available computing, storage, and networking physical resources to support multiple concurrent tenants in an isolated way; as well as, (iv) the provisioning of homogeneous Application Programming Interfaces (APIs) atop heterogeneous GU-dependent physical devices. However, the attainment of these benefits is currently hampered by at least three *still open* challenges [41,18]. First, being the controller of centralized type, SDN/NFV-based architectures require that *both* data and control planes are highly reliable. Second, implementing the control plane in a centralized way introduces *both* further computing and networking overheads. Specifically, the GCS of Fig. 1 consumes computing resources *both* for maintaining an updated global view of the GU-UAV link states and, then, dynamically planning resource re-configuration decisions. Afterwards, the elaborated decisions must be communicated to the UAV and GUs, thus consuming further network resources. Third, the resources hosted by the serving UAV are typically limited in terms of computing power, network bandwidth, storage size, and above all, the available energy budget for their supplying is severely constrained. In this regard, we point out the main goal of the proposed joint co-design of the GCS and UAV virtualized architectures in Section 6.2 is to address these open challenges. The final goal is to provide orchestration support for the execution of the (virtualiazed) microservices possibly offloaded by the served GUs [40].

Overall, the conducted overview, confirms that our proposal is unique in:

- performing the 3D optimization of the trajectory parameters of the RW-UAV in the hotspot scenario of Fig. 1, where the (non-convex) acceleration-dependent energy propulsion model and the (non-convex) constraints enforced by the adopted probabilistic path loss, UAV antenna beam-width, and maximum tolerated outage probability are *simultaneously* taken into account; and,
- developing a *joint co-design* of the virtualized computing/communication architectures of both GCS and UAV, in order to allow the orchestration of the virtualized services required by GUs even in the presence of GCS failures.

3. System modeling

We consider the cellular layout of Fig. 1, in which a mobile RW-UAV acts as a flying server to provide wireless access and/or service orchestration to a number of GUs equipped with (possibly) heterogeneous computing/communication capabilities.

Similar to [42,43], we assume that the GUs are randomly, *evenly*, and independently distributed with a given spatial density $\lambda\left(\text{user}/\text{m}^2\right)$ over a circular area with a radius of $R_C\,(\text{m})$. Hence, the *average* total number of GUs, served by the UAV, is: $\overline{N}_U = \lambda\ \pi\ R_C^2\,(\text{user})$. By definition, hotspot scenarios are characterized by high values of λ, we say [42]: $\lambda \geq\ 10^{-3}\ \left(\text{user}/\text{m}^2\right)$. Furthermore, in Fig. 1, the GUs may be fixed or mobile. In both cases, the GUs locations and their exact number are neither known in advance nor predictable. These assumptions feature typical hotspot scenarios, in which localization support (like GPS-based radio localization support) from fixed infrastructure is not available or even unfeasible at all, due to the large value of λ [42, Section IV.E], [43]. The serving UAV cyclically flies at an altitude H (m) and with linear speed of $v \triangleq \|\vec{v}\|\,(\text{m}/\text{s})$ along a circular trajectory of radius $R\,(\text{m})$. All the trajectory parameters H, v, and R are assumed fixed but adjustable. The projection of the center of the UAV trajectory onto the ground coincides with both the center of the coverage area and the origin of the adopted Cartesian reference system (see Fig. 1).

UAV roles and supported services In the considered framework of Fig. 1, the flying UAV may serve as both: (i) a Base Station (BS), in order to allow GUs to access the remote Internet by using the UAV as local Gate-Way (GW); as well as, (ii) a Fog Computing Node (FCN), in order to allow service offloading in form of Virtual Machines (VMs)/Containers (CONs) from resource-poor GUs. In this regard, we note that, since we are mainly interested to the case in which the UAV acts as a flying communication and/or computing server, the uplink communication from the GUs to the UAV is the main focus. However, we anticipate that, from a formal point of view, the problem formulation of Section 3.3 (and, then, the resulting optimized solution of Section 4) would *apply verbatim* to the companion case in which the UAV would act as information disseminator and, then, the focus would shift to the downlink communication from the UAV to the GUs. According to these considerations, we assume that each GU of Fig. 1 may directly communicate with the serving UAV by exploiting the underlying single-hop terrestrial-aerial bi-directional short-range link, but he cannot establish a direct multi-hop long-range link to the remote Internet. When it is present, the main twofold roles of the GCS are to act as global Internet Gateway, as well as central Controller for the UAV. Since UAV-GCS communication is assumed to exploit out-of-band signaling over the wireless backhaul of Fig. 1, the resulting UAV-GU and UAV-GCS links are not affected by co-channel interference.

Adopting circular UAV trajectory in hotspot scenarios As pointed out in [42,22–25], there are at least four main reasons for adopting a UAV circular trajectory in the considered hotspot scenario of Fig. 1. First, since both the actual number of GUs and their locations are unknown and even unpredictably time-varying, pursuing UAV trajectory planning that depends on the number and locations of the served GUs is, indeed, unfeasible. Second, although UAVs may hover aloft, nevertheless, this is not the most energy-saving flying state [11]. Third, the comparative analysis carried out in [42,22] supports the general conclusion that circular trajectories with jointly optimized radii/speeds/altitudes are capable of approaching the maximum energy efficiency over the family of the *cyclic* trajectories. Forth, under the assumption of evenly and randomly distributed GUs, the considerations reported, for example, in [42, Section IV.E.2] lead to the conclusion that a circular UAV trajectory with optimized radius/altitude/speed parameters may effectively shorten the spatial and time-averaged UAV-GU distance to decrease the resulting average path-loss experienced by the GUs.

Utilizing RW-UAV in hotspot scenarios As pointed out in [11], an RW-UAV is equipped with propellers that enable it to: (i) move up/down along the vertical spatial direction; (ii) stay aloft in the air; and (iii) move over the horizontal 2D plane. These native features give more flexibility in location of RW-UAVs and make their utilization very interesting as flying base stations and/or Fog nodes, especially when dedicated runways are not present and vertical taking off/landing is demanded. However, the propulsion-energy consumption of RW-UAVs may be larger than the ones of similar size FW-UAVs so that the energy-saving optimization of the RW-UAV 3D trajectories becomes an imperative task.

3.1. Adopted probabilistic path-loss model

In the considered scenario of Fig. 1, we assume that the serving UAV is equipped with a single transmit/receive directional antenna, whose gain $G_{UAV}(\phi)$ (in linear scale) may be expressed as a function of the elevation angle $\phi\,(\text{deg})$ as in [7,10]:

$$G_{UAV}(\phi) = \begin{cases} G_0\,, & -\Phi_{UAV} \leq \phi \leq +\Phi_{UAV}\,, \\ \cong 0\,, & \text{otherwise}, \end{cases} \tag{1}$$

where (see Fig. 1): $\Phi_{UAV} \in (0, 90)$ is the semi half-power elevation antenna beamwidth (measured in (deg)), while [7,10]:

$$G_0 \cong \frac{2.9 \times 10^4}{\left(2 \times \Phi_{UAV}\right)^2}, \tag{2}$$

is the corresponding gain (in linear scale) of the antenna radiation main lobe. Furthermore, without loss of generality, we also assume that each GU is equipped with a radio transceiver, whose antenna is omni-directional and unit-gain [10].

Regarding the GU-UAV up/down wireless links, in this paper, we consider the (standard) probabilistic channel model in [19], in which the link alternates (in an *unpredictable* way) LoS and $NLoS$ states. Since the trajectory of the serving UAV follows a periodic pattern, short-term random fluctuations average out and it is expected that the resulting per-user ground-air channels are mainly affected by long-term time variations [19]. Hence, like [42,22,11,43] and the references therein, we can neglect fast-fading effects and focus on shadowing and slow fading-induced channel variations. Although these last ones may exhibit random behaviors, due to their slow-variant nature, we can only consider their mean values, because coverage planning typically embraces large horizon times [11,43]. From now on, the mean value (in linear scale) of the additional path loss for LoS and $NLoS$ terrestrial-aerial link between each GU and the serving UAV are denoted by η_{LoS} and η_{NLoS} respectively, with $\eta_{NLoS} > \eta_{LoS} \geq 1$.

Although, at each instant, a ground-air channel is either LoS or $NLoS$, we also observe that, under the adopted channel model, the path-loss is obtained by averaging both states according to their occurrence probabilities to provide an average channel description that is neither LoS nor $NLoS$. In fact, for the purpose of optimization, it is virtually infeasible to distinguish between LoS and $NLoS$ states, because the ground-air links are affected by random phenomena induced by both GU mobility patterns and unpredictable environmental factors (like blocking phenomena due to buildings or moving obstacles). As a

consequence, since the $LoS/NLoS$ per-GU link conditions may considerably change due to slight displacements of the UAV and/or GUs, there is no way to identify whether a target ground-air link is LoS or $NLoS$ before the spatial deployments of the UAV and target GUs. Furthermore, since in hot-spot scenarios, the number of GUs can be high and time-varying, the instantaneous tracking of the $LoS/NLoS$ states of all per-GU ground-air links is a challenging task that may require a lot of signaling control flows [42–45]. Because of these considerations, hereafter we utilize the per-GU average path-loss for characterizing the corresponding average link attenuation factor [7,10].

Let $\left(p_K(t), \psi_K(t), 0\right)$, and $\left(R, \psi_{UAV}(t), H\right)$ be the 3D polar coordinates of the (mobile) K-th GU (GU#K) and the serving UAV at time t under the Cartesian reference system of Fig. 1. Hence, the resulting instantaneous distance $d_K(t)$ (measured in (m)) between $GU\#K$ and the UAV and the corresponding elevation angle $\theta_K(t)$ (measured in (deg)) reads as:

$$d_K(t) = \sqrt{H^2 + {r_K}^2(t)}, \qquad \text{and}: \qquad \theta_K(t) = \arctan\left(H/r_K(t)\right), \tag{3}$$

where:

$$r_K(t) = \sqrt{{p_K}^2 + R^2 - 2Rp_K(t)\cos\left(\psi_K(t) - \psi(t)\right)}, \tag{4}$$

is the planar distance (in (m)) between the instantaneous position of $GU\#K$ and the projection onto the ground of the corresponding instantaneous position of the serving UAV (See Fig. 1). Since the resulting LoS probability, experienced by $GU\#K$

$$P_{LoS}\left(\theta_K(t)\right): \quad [0,\ 90] \rightarrow [0,\ 1], \tag{5}$$

also depends on the instantaneous value of the elevation angle [7,10], it is time-varying. Regarding the behavior of $P_{LoS}(\theta)$ as a function of the elevation angle θ, the common assumption behind the various analytical models proposed in the literature is that $P_{LoS}(\theta)$ is strictly increasing in θ (see [2,7,10] for recent overviews on this topic). Hence, we only use this (mild) assumption about the analytical behavior of the actually adopted LoS probability model in Eq. (5).

The instantaneous path loss (in linear scale): $L_m^{(K)}(t)$, $m \in \{LoS, NLoS\}$, experienced by the link between the serving UAV and $GU\#K$ in the $LoS/NLoS$ operating conditions, depends on the corresponding distance in Eq. (3) as in [7]:

$$L_m^{(K)}(t) = \eta_m \left(4\pi f_c d_K(t)/c\right)^{\delta}, \quad m \in \{LoS, NLoS\}, \tag{6}$$

where c (m/s) is the light speed, f_c (Hz) is the carrier frequency, δ is the (dimensionless) path loss exponent, and η_ζ is the (previously introduced) excessive path loss (in linear scale) that depends on the presence/absence of the LoS path. For this reason, like the work in [42,43], we use the instantaneous *averaged* path loss:

$$\overline{L}^{(K)}(t) = L_{LoS}^{(K)}(t)\, P_{LoS}\left(\theta_K(t)\right) + L_{NLoS}^{(K)}(t)\left(1 - P_{LoS}\left(\theta_K(t)\right)\right), \tag{7}$$

to characterize the resulting instantaneous average link gain: $\overline{g}^{(K)}(t) \triangleq \left(\overline{L}^{(K)}(t)\right)^{-1}$ experienced by $GU\#K$.

Worst-case average path-loss The average path loss in Eq. (7) depends on the instantaneous 3D relative position of the (mobile) UAV to the considered GU so that it is time-varying and depends on the GU index K. This means each GU may require its own optimized UAV altitude to minimize the experienced average path-loss. Since the per-GU optimization of the UAV altitude is unfeasible, we use as upper bound the *worst-case* average path-loss that is experienced by the *full* set of the served GUs at *every* instant to guarantee all the GUs a maximum average path-loss at every instant. Like [43], the reason for pursuing this worst-case planning approach is that the coverage provided by the serving UAV must be *always-on* and *ubiquitous*, and must be guaranteed *even* in the worst-case to support per-GU real-time services. Towards this end, the full set of the planar distances in Eq. (4) is upper bounded by (see Fig. 1): $r^{(MAX)} = R + R_C$ so that the UAV-GU distances and elevation angles in Eq. (3) maintain upper and lower-bounded as in:

$$\begin{aligned} &d_K(t) \le d^{(MAX)} \triangleq \left(H^2 + \left(R + R_c\right)^2\right)^{\frac{1}{2}} \quad \text{and} \\ &\theta_K(t) \ge \theta^{(MAX)} \triangleq \arctan\left(\frac{H}{R + R_c}\right). \end{aligned} \tag{8}$$

Hence, since $\overline{L}^{(K)}(t)$ in Eq. (7) is, by design, an increasing (resp., decreasing) function of $d_K(t)$ (resp., $\theta_K(t)$), the following upper bound directly follows from Eqs. (6) and (7):

$$\begin{aligned} \overline{L}^{(K)}(t) &\le \overline{L}^{(MAX)} \\ &\triangleq K_0 \left(d^{(MAX)}\right)^{\delta} \left[\eta_{NLoS} - \left(\eta_{NLoS} - \eta_{LoS}\right) P_{LoS}\left(\theta^{(MIN)}\right)\right], \end{aligned} \tag{9}$$

where: $P_{LoS}\left(\theta^{(MIN)}\right)$ indicates the values assumed by the LoS probability function at the elevation angle $\theta^{(MIN)}$, while

$$K_0 \triangleq \frac{1}{G_0}\left(\frac{4\pi f_c}{c}\right)^{\delta}, \tag{10}$$

is a dummy constant that depends on the UAV antenna gain of Eq. (2) and the operating carrier frequency. A direct inspection of Fig. 1 leads to the conclusion that $\overline{L}^{(MAX)}$ in Eq. (9) is the average instantaneous path loss *actually* experienced by a GU, that is placed on the boundary of the coverage region, when the projection onto the ground of the current position of the UAV is on the straight line that joins the GU to the origin of the underlying reference system (see $GU\#1$ in Fig. 1).

3.2. Adopted acceleration-dependent propulsion power-energy models

In the recent contributions [13,14], a formula for the analytical modeling of the propulsion power: $\mathscr{P}_p^{(RW)}$ (W) of a RW-UAV is proposed and validated, which explicitly takes into account for *both* the speed: $\vec{v}$ and the acceleration: $\vec{a}$ vectors of the aircraft. It generalizes the formula previously presented in [11] for the (more particular) case of acceleration-*free* RW-UAV motion (see also [2] for a recent review on the propulsion power/energy consumption models of RW-UAVs). Hence, according to [13, Eq. (4)], in the considered case of RW-UAV flight level (i.e. fixed altitude), this acceleration-dependent power formula reads as follows:

$$\begin{aligned} \mathscr{P}_p^{(RW)} = &\underbrace{\gamma_1\left(1 + \gamma_2 \left\|\vec{v}\right\|^2\right)}_{\text{Blade power}} + \underbrace{\gamma_3 \left\|\vec{v}\right\|^3}_{\text{Parasite power}} \\ &\underbrace{+\gamma_4 \left[\left(1 + \frac{\left\|\vec{a}_c\right\|^2}{g^2}\right) \times \left(\left(1 + \frac{\left\|\vec{a}_c\right\|^2}{g^2} + \frac{\left\|\vec{v}\right\|^4}{\gamma_5^2}\right)^{\frac{1}{2}} - \frac{\left\|\vec{v}\right\|^2}{\gamma_5}\right)\right]^{\frac{1}{2}}}_{\text{Induced power}}, \end{aligned} \tag{11}$$

where [2,13,14]: (i) γ_1 (W), γ_2 $\left((\text{m/s})^{-2}\right)$, γ_3 $\left((\text{m/s})^{-3} \times \text{W}\right)$, γ_4 (W), and γ_5 $\left((\text{m/s})^2\right)$ are positive constants, which depend on the aerodynamic properties and mechanical structural features of the considered RW-UAV [11,13]; (ii) $g \equiv 9.81$ $\left(\text{m/s}^2\right)$ is the gravitational acceleration; and, (iii) $\vec{v}$ (m/s) and $\vec{a}_c$ $\left(\text{m/s}^2\right)$ are the (instantaneous) speed and centrifugal acceleration vectors of the RW-UAV.

The propulsion power model in Eq. (11) is the summation of three power terms, namely,

(i) the blade profile power, which scales up as the squared modulus: v^2 of the speed vector. It accounts for the power required to compensate the mechanical profile drag induced by the rotation of the blades;

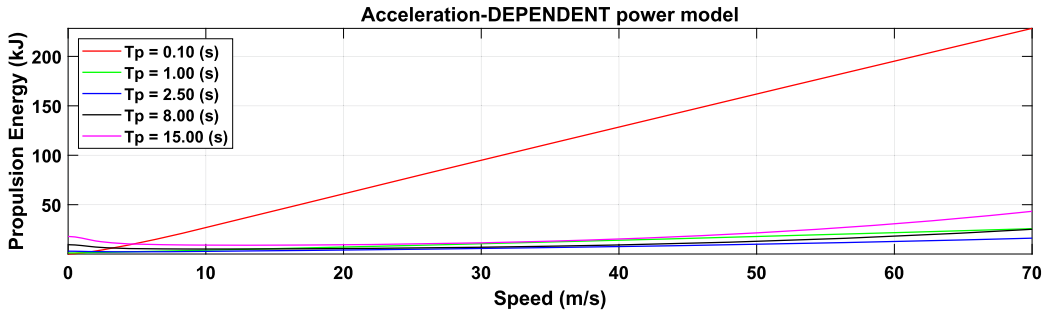

(a)

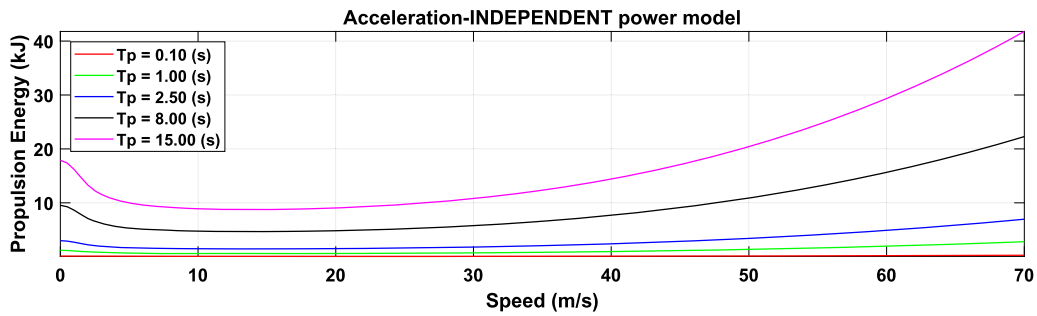

(b)

Fig. 2. (a) $\mathscr{E}_P^{(RW)}$-vs.-v behaviors at T_P of 0.1 (s), 1.0 (s), 2.5 (s), 8.0 (s), and 15.0 (s) under [13]: $\gamma_1 = 504.60\,(\mathrm{W})$, $\gamma_2 = 6.53 \times 10^{-5}\left((\mathrm{m/s})^{-2}\right)$, $\gamma_3 = 6.35 \times 10^{-3}\left((\mathrm{m/s})^{-3} \times \mathrm{W}\right)$, $\gamma_4 = 687.88\,(\mathrm{W})$, and $\gamma_5 = 90.20\left((\mathrm{m/s})^2\right)$; (b) Corresponding behaviors when the acceleration-dependent terms in Eq. (11) are (erroneously) ablated. Case of circular trajectory at constant altitude and speed.

(ii) the parasite power, which scales up as the third power: v^3 of the modulus of the speed vector. It accounts for the power required to compensate the parasitic friction drag induced by the UAV movement in the air; and

(iii) the induced power, which depends on both the speed and centrifugal acceleration vectors. It accounts for the power required to compensate for the induced drag that is developed by the generation of the lift force needed to maintain the UAV airborne.

By passing Eq. (11) to the limit for vanishing speed and acceleration, we obtain the (finite-valued) power:

$$\mathscr{P}_H^{(RW)} \triangleq \mathscr{P}_p^{(RW)}\Big|_{\substack{\|\vec{v}\|=0\\ \|\vec{a}_c\|=0}} \equiv \gamma_1 + \gamma_4, \tag{12}$$

that the RW-UAV wastes to stay aloft in the air.

As pointed out in [13], the key distinguishing feature of the power model in Eq. (11) is the presence of the two 'square root' terms in the expression of the induced power, which depend on the modulus: a_c of the centrifugal acceleration vector $\vec{a}_c$. Since this last one equates to:

$$a_c \triangleq \|\vec{a}_c\| = \left(\|\vec{a}\|^2 - \frac{\left(\vec{a}^T\vec{v}\right)^2}{\|\vec{v}\|^2}\right)^{\frac{1}{2}}, \tag{13}$$

the modulus of the component of the overall acceleration vector $\vec{a}$ that is normal to the velocity vector $\vec{v}$, it accounts for the power that the RW-UAV wastes for its heading changes. As a consequence of this presence, the model in Eq. (11) may apply to every trajectory followed by a RW-UAV that flights at constant altitude. Specifically, in the considered case of circular trajectory at constant speed, we have:

$$v = \omega R \equiv \frac{2\pi R}{T_P} \qquad \text{and} \qquad a_c = \omega^2 R \equiv \frac{2\pi v}{T_P}, \tag{14}$$

where: $2\pi/T_P\,(\mathrm{rad/s})$ is the UAV angular velocity and $T_P\,(\mathrm{s})$ is the associated trajectory period.

We note that the presence of the acceleration-dependent terms in Eq. (11) not only does more challenging the formal approaches to be pursued for solving optimization problems based on the model in Eq. (11) but also deeply impacts on the resulting solutions. Just to gain some first insights about the impact of the centrifugal acceleration terms in Eq. (11), Fig. 2a reports the numerically evaluated behaviors of the resulting per-period propulsion energy:

$$\mathscr{E}_P^{(RW)} \triangleq \mathscr{P}_P^{(RW)}\, T_P, \tag{15}$$

as function of v at various T_P values in the case of circular trajectory at constant speed and altitude. For comparison purpose, Fig. 2b shows the corresponding per-period energy behaviors when the acceleration-dependent terms in Eq. (11) are (erroneously) neglected, i.e., they are set to zero.

A comparison of the plots of Figs. 2a and 2b leads to four main conclusions.

First, according to Eq. (15), the only effect of T_P in the acceleration-independent case is to merely scale up/down the corresponding energy profiles. In particular, the energy profiles of Fig. 2b scale proportionally to T_P and approach zero for vanishing T_P values. This scaling trend is no longer retained by the corresponding energy curves of Fig. 2a. In fact, due to the dependence of the centrifugal acceleration in Eq. (14) on T_P, the shapes of the energy plots of Fig. 2a substantially vary with T_P and (most importantly) they no longer vanish for vanishing T_P (e.g., compare the increasing behaviors of the red and green curves of Fig. 2a with the corresponding ones of Fig. 2b).

Second, due to these contrasting behaviors, the plots at lower T_P values of Fig. 2a cross the corresponding ones at higher T_P's at speeds exceeding 4 - 5 (m/s), while crossing points are not presented in the set of the corresponding plots of Fig. 2b.

Third, as it could be expected, the behaviors of the energy plots of Fig. 2a become more similar to the corresponding ones of Fig. 2b at

higher T_P values, that is, when the effects of the acceleration-dependent terms in Eq. (11) become more negligible (e.g. compare the black and magenta plots of Fig. 2a with the corresponding ones of Fig. 2b).

Forth, all the plots reported in Fig. 2 tend to attain their minimum values at non-vanishing speeds. As already noted, this confirms that staying aloft in the air is not the most energy-efficient state for typical RW-UAVs [11], especially when the trajectory periods are larger than a few seconds.

Hereafter, we focus on the optimization of the UAV propulsion energy $\mathscr{E}_P^{(RW)}$ in Eq. (15), because the plots of Fig. 2a confirm that the propulsion energy consumption is of the order of kJ's, while the corresponding communication-induced energy wasting is typically beyond 100 times smaller (see [7,10,46,45] and the references therein).

3.3. System constraints

In this section, we introduce and motivate the system constraints, considered in the minimization of the per-period propulsion energy of Eq. (15).

The first two constraints are of box-type and concern the allowed maximum and minimum radius and altitude of the UAV trajectory. As it is required by GP [47], they can be directly formulated in the following monomial forms[2]:

$$0 \leq \frac{R}{R_C} \leq 1, \quad H^{(MIN)} H^{-1} \leq 1, \quad \text{and} \quad \frac{H}{H^{(MAX)}} \leq 1. \tag{16}$$

The vanishing lower bound on R accounts for the fact that a RW-UAV may stay aloft in the air at the center of the coverage area of Fig. 1, while the $H^{(MAX)}$ and $H^{(MIN)}$ - enforced upper and lower bounds on H are jointly dictated by regulatory rules and constraints on the maximum coverage of the employed radio technology [2].

The third constraint accounts for the finite beam-width in Eq. (1) of the UAV antenna. It involves both the trajectory radius and altitude. Since it reads as in (see Fig. 1): $(R + R_C) \leq H \tan\left(\Phi_{UAV}\right)$, it can be equivalently formulated in the following posynomial form:

$$\frac{R H^{-1}}{\tan\left(\Phi_{UAV}\right)} + \frac{R_C H^{-1}}{\tan\left(\Phi_{UAV}\right)} \leq 1. \tag{17}$$

Under the assumption that the UAV antenna is tilted towards the ground, Eq. (17) guarantees that the antenna beam-width of the RW-UAV of Fig. 1 always covers all the GUs that fall into the coverage area of Fig. 1, regardless of the instantaneous position of the UAV along the followed circular trajectory.

The fourth and fifth constraints involve the maximum allowed UAV speed and trajectory period and they may be directly formulated in the following monomial forms:

$$0 \leq \frac{v}{v^{(MAX)}} \equiv \frac{2\pi R T_P^{-1}}{v^{(MAX)}} \leq 1 \qquad \text{and} \qquad 0 \leq \frac{T_P}{T_P^{(MAX)}} \leq 1. \tag{18}$$

The $v^{(MAX)}$ - dictated upper bound on the UAV speed is due to mechanical constraints,[3] while the $T_P^{(MAX)}$ - enforced upper bound on the trajectory period arises from the requirement that the periodic fluctuations of the per-GU instantaneous path losses in Eq. (7) due to the circular motion of the serving UAV average fast enough to guarantee adequate averaged terrestrial-aerial link gains [2].

The last constraint involves the previously introduced worst-case averaged path loss in Eq. (9). After indicating by TH_{PL} the maximum tolerated path loss threshold (in linear scale), the resulting constraint reads as in (see Eq. (9)):

$$K_0 \left(d^{(MAX)}\right)^{\delta} \left[\eta_{NLoS} - \left(\eta_{NLoS} - \eta_{LoS}\right) P_{LoS}\left(\theta^{(MIN)}\right)\right] \leq TH_{PL}. \tag{19}$$

However, this constraint may not be sufficient to guarantee the QoS-dictated communication throughput that is required for some delay-sensitive real-time applications like video-streaming or real-time monitoring applications [48]. Since η_{NLoS} in Eq. (19) is typically larger than the corresponding η_{LoS} of beyond 100 times [10,19], it is likelihood to retain that each per-GU terrestrial-aerial link is out-of-service when it operates in the $NLoS$ state. Hence, concerning practical cases, it may be reasonable to enforce that the $P_{LoS}\left(\theta^{(MIN)}\right)$ term present in Eq. (19) is not smaller than a target in-service probability: $P_{SER} \equiv 1 - P_{OUT}$, where P_{OUT} plays the dual role of maximum tolerated outage probability. Therefore, it may be reasonable to replace the (single) constraint in Eq. (19) by the following coupled constraints:

$$P_{LoS}\left(\theta^{(MIN)}\right) \geq P_{SER}, \tag{20}$$

and

$$K_0 \left(d^{(MAX)}\right)^{\delta} \left[\eta_{NLoS} - \left(\eta_{NLoS} - \eta_{LoS}\right) P_{SER}\right] \leq TH_{PL}. \tag{21}$$

Remark 1 *(On the role of the constraints in Eqs. (20) and (21), and related network stability issues).* Before proceeding, we note that the pairs of constraints in Eqs. (20) and (21) are stronger than the single constraint in Eq. (19), because $P_{LoS}(\theta^{(MIN)})$ in Eq. (19) is replaced with its lower bound: $P_{SER} \equiv 1 - P_{OUT}$. However, the constraint in Eq. (20) on the minimum allowed $P_{LoS}(\theta^{(MIN)})$ plays the role of minimum in-service probability to be guaranteed by all aerial-terrestrial links of Fig. 1, and it represents a QoS-dictated constraint. Furthermore, we have experienced that it is very challenging to derive a lower-bound in closed-form: $\Psi(\theta^{(MIN)})$ on $P_{LoS}(\theta^{(MIN)})$ in Eq. (20), which is: (i) polynomial in $\theta^{(MIN)}$, to be utilized in the pursued GP solving approach of Section 5; (ii) increasing in $\theta^{(MIN)}$ to mimic the same monotonic behavior of $P_{LoS}(\theta^{(MIN)})$; and (iii) concave in $\theta^{(MIN)}$ to make convex the constraint in Eq. (20). This negative result does not allow us to manage: $P_{SER} \equiv 1 - P_{OUT}$ in Eqs. (20) and (21) as a slack variable to optimize. However, in Section 7, we will numerically evaluate the energy loss that is induced by the replacement of the constraint in Eq. (19) by the coupled ones of Eqs. (20) and (21) as well as the resulting energy loss sensitivity on the target P_{SER}. In this regard, we further note that, since the focus of the reference framework of Fig. 1 is on providing aerial radio coverage to the GUs in the presence of path-loss induced by slow-fading phenomena (see Section 2), queueing aspects and related (possibly, randomly time-varying) queue delays are, by design, not considered. However, we note that the constraint in Eq. (21) on the worst-case average path-loss combined to the setting of the corresponding threshold TH_{PL} reported in Eq. (50) enforces *network stability*, e.g., it suffices to guarantee that each GU may attain own average target bit-rate even in the presence of multiple-access interference and/or GU heterogeneity (see the analysis of Section 6.1).

Afterwards, after denoting by:

$$P_{LoS}^{-1}(w): \ [0\,,1] \rightarrow [0\,,90], \tag{22}$$

the (strictly increasing and monotonic-preserving) inverse function of the LoS probability function $P_{LoS}(\theta)$,[4] the coupled constraints in Eqs. (20) and (21) may be re-cast in the following equivalent posynomial forms:

$$A_0 \ H^{-1}(R + R_C) - 1 \leq 0, \tag{23}$$

and

[2] See [47, Section 11.5] for the formal definitions of GP and monomial/posynomial functions. In this regard, we point out that: $\tan\left(\Phi_{UAV}\right)$ in Eq. (17.1) is guaranteed to be non-negative, because, by definition, $0° \leq \Phi_{UAV} \leq 90°$.

[3] The maximum speed of state-of-the-art small size RW-UAVs is typically limited up to $60 - 70\,(\mathrm{m/s})$ [7,10].

[4] Since $P_{LoS}(\theta)$ is strictly increasing by assumption, it admits the (strictly increasing) inverse function of Eq. (22).

$$B_0\left(H^2+R^2+2R_CR+R_C^2\right)-1\leq 0. \tag{24}$$

The (positive) dummy constants:

$$A_0 \triangleq \tan\left(P_{LoS}^{-1}\left(P_{SER}\right)\right), \quad \text{and :}$$
$$B_0 \triangleq \left[\frac{K_0\left(\eta_{NLoS}-\left(\eta_{NLoS}-\eta_{LoS}\right)P_{SER}\right)}{TH_{PL}}\right]^{2/\delta}, \tag{25}$$

account for the aggregate effect of the (previously introduced) *LoS* probability model, required in-service target probability and allowed path loss threshold.

4. Problem statement and feasibility conditions

The formal statement of the afforded optimization problem reads as follows:

$$\textbf{P1:} \quad \min_{\{R,\,H,\,T_P\}} \quad \mathscr{E}_P^{(RW)}, \tag{26a}$$
$$\text{s.t.:} \quad \text{Eqs. (16), (17), (18), (23), and (24),} \tag{26b}$$

where the per-period propulsion energy is defined in Eq. (15) with the corresponding acceleration-dependent propulsion power given by Eq. (11).

All the constraints of the afforded problem are convex and, as it is required by the GP, they are already in posynomial or monomial form. However, the current form of the energy objective function in Eq. (15) is *neither* convex *nor* posynomial. In Section 5, we proceed to convexify the function $\mathscr{E}_P^{(RW)}$ in Eq. (26a) by introducing a suitable set of auxiliary slack variables and associated constraints. However, using the slack variables is merely a means to rewrite the objective function in Eq. (26a) in a suitable parametric form (see [47, Chapter 2]). Hence, their introduction does not modify neither the feasibility conditions nor the Slater's qualification conditions of the original P1 problem, which continue to be dictated only by the set of constraints in Eq. (26b). Motivated by this consideration, in the remaining part of this Section 4, we study the feasibility of this set of constraints.

4.1. Feasibility conditions

We note that the box constraints on the allowed UAV speed and trajectory period in Eq. (18) are always feasible but they introduce an upper bound on the allowed values of the trajectory radius. This is because their joint action enforces the following upper bound on the allowed R's values (see Eq. (18)):

$$R\leq \frac{v^{(MAX)}\,T_P}{2\pi}\leq \frac{v^{(MAX)}\,T_P^{(MAX)}}{2\pi}. \tag{27}$$

Since R may be vanishing (see Eq. (16)), the last inequality in Eq. (27) guarantees that the couple of constraints in Eq. (18) remains feasible under every (possibly, vanishing) value of $v^{(MAX)}$ and $T_P^{(MAX)}$, but it limits the range of the allowed trajectory radii. Furthermore, the upper bound in Eq. (27) proves that the RW-UAV of Fig. 1 is forced to stay aloft in the air when $v^{(MAX)}$ and/or $T_P^{(MAX)}$ vanish.

The necessary and sufficient conditions for the feasibility of the remaining constraints listed in Eq. (26b) are reported in the following *Propositions* 1, 2 and 3, whose proofs are detailed in Appendix B.

Proposition 1 *(On the feasibility of the constraints in Eqs. (16) and (17)). Under the previously considered constraints in Eq. (18), a necessary and sufficient condition for the joint feasibility of the set of constraints in Eqs. (16) and (17) is that the following inequality is met:*

$$H^{(MAX)}\tan\left(\Phi_{UAV}\right)-\min\left\{R_C\,;\,\frac{v^{(MAX)}\,T_P^{(MAX)}}{2\pi}\right\}\geq 0. \tag{28}$$

■

Proposition 2 *(On the feasibility of the constraint in Eq. (23)). Let us assume that the target in-service probability P_{SER} in Eq. (20) falls in the domain allowed the considered LoS probability function, that is, let us assume that:*

$$P_{LoS}(0)\triangleq P_{SER}^{(MIN)}\leq P_{SER}\leq P_{SER}^{(MAX)}\triangleq P_{LoS}(90). \tag{29}$$

Hence, under the previously considered constraints in Eqs. (16), (17) and (18), we have that:

(a) *a necessary condition for the feasibility of the constraint in Eq. (23) is that the following inequality is met:*

$$H^{(MAX)}\geq A_0\;R_C, \tag{30}$$

with A_0 defined as in Eq. (25);

(b) *a sufficient condition for the feasibility of the constraint in Eq. (23) is:*

$$H^{(MIN)}\geq A_0\;\left(R_C+R^{(MAX)}\right), \tag{31}$$

with the (nonnegative) constant $R^{(MAX)}$ defined as in (see Appendix B):

$$R^{(MAX)}\triangleq \min\left\{H^{(MAX)}\tan\left(\Phi_{UAV}\right)-\min\left\{\frac{v^{(MAX)}\,T_P^{(MAX)}}{2\pi};R_C\right\};R_C\right\}. \tag{32}$$

■

Proposition 3 *(On the feasibility of the constraint in Eq. (24)). Under the previously considered constraints in Eqs. (16), (17), (18) and (23), we have that:*

(a) *a necessary condition for the feasibility of the constraint in Eq. (24) is that the following inequality is met:*

$$\left(H^{(MIN)}\right)^2+R_C^2\leq \frac{1}{B_0}, \tag{33}$$

with B_0 defined as in Eq. (25);

(b) *a sufficient condition for the feasibility of the constraint in Eq. (24) is:*

$$\left(H^{(MAX)}\right)^2+\left(R_C+R^{(MAX)}\right)^2\leq \frac{1}{B_0}, \tag{34}$$

with $R^{(MAX)}$ given by Eq. (32). ■

Before proceeding, two remarks about the meaning/role of the reported feasibility conditions are in order. First, although the constraints in Eq. (18) are always feasible, they upper bound the allowed maximum radius: $R^{(MAX)}$ in Eq. (32). Furthermore, their presence affects the optimized values of the UAV propulsion energy in Eq. (26). Second, the (intuitive) reason why is challenging (if feasible at all) to develop conditions that are simultaneously necessary and sufficient for the feasibility of the constraints in Eqs. (23) and (24) is that they exhibit contrasting behaviors as functions of R and H. Specifically, the function at the l.h.s. of Eq. (23) increases (resp., decreases) for increasing H (resp., R), while the l.h.s. of Eq. (24) is jointly increasing in H and R.

5. Proposed solving approach

The main goal of this section is to re-cast the propulsion energy function of Eq. (15) in posynomial form so to turn the resulting constrained optimization problem of Eq. (26) in GP form. To this end, in the Appendix C, we develop a (seemingly new) formal procedure, which is *ad hoc* tailored to convexify the acceleration-dependent terms of the propulsion power model of Eq. (11). This is done by introducing two suitable slack variables (the positive and scalar-valued slack variables y and z of Eqs. (C.1) and (C.2)), together with two associated slack con-

straints (the auxiliary constraints of Eqs. (C.7) and (C.8)). Therefore, after introducing the five-dimensional column vector:

$$\vec{\tilde{X}} \triangleq \left[\tilde{R},\ \tilde{H},\ \tilde{T}_P,\ \tilde{y},\ \tilde{z}\ \right]^T \triangleq \left[\log R,\ \log H,\ \log T_P,\ \log y,\ \log z\ \right]^T, \quad (35)$$

of the log-transformed versions of all the resulting trajectory dependent-plus-slack optimization variables, the developments reported in Appendix C prove that the optimization problem P1 may be turned into the following one:

$$\textbf{P2:} \quad \min_{\vec{\tilde{X}}} \quad \mathscr{E}_P^{(RW)}\left(\vec{\tilde{X}}\right), \quad (36a)$$

s.t.:

$$\phi_1\left(\vec{\tilde{X}}\right) \triangleq \frac{1}{c_0}\exp\left(-\left(4\tilde{z}+2\tilde{y}\right)\right)-1 \le 0, \quad (36b)$$

$$\phi_2\left(\vec{\tilde{X}}\right) \triangleq \exp\left(2\tilde{y}\right)+\frac{(2\pi)^4}{g^2}\exp\left(2\tilde{R}+2\tilde{y}-4\tilde{T}_P\right)-1 \le 0, \quad (36c)$$

$$\tilde{R} \le \log R_C, \quad (36d)$$

$$\log H^{(MIN)} \le \tilde{H} \le \log H^{(MAX)}, \quad (36e)$$

$$\tilde{T}_P \le \log T_P^{(MAX)}, \quad (36f)$$

$$\phi_3\left(\vec{\tilde{X}}\right) \triangleq \frac{1}{\tan\left(\Phi_{UAV}\right)}\exp\left(-\tilde{H}\right)\left[\exp\left(\tilde{R}\right)+R_C\right]-1 \le 0, \quad (36g)$$

$$\phi_4\left(\vec{\tilde{X}}\right) \triangleq A_0\exp\left(-\tilde{H}\right)\left[\exp\left(\tilde{R}\right)+R_C\right]-1 \le 0, \quad (36h)$$

$$\phi_5\left(\vec{\tilde{X}}\right) \triangleq B_0\left[\exp\left(2\tilde{R}\right)+\exp\left(2\tilde{H}\right)+2\ R_C\exp\left(\tilde{R}\right)+R_C^2\right]-1 \le 0, \quad (36i)$$

$$\phi_6\left(\vec{\tilde{X}}\right) \triangleq \frac{2\pi}{v^{(MAX)}}\exp\left(\tilde{R}-\tilde{T}_P\right)-1 \le 0. \quad (36j)$$

In the reported formulation of the P2 problem, we have that:

(i) the energy objective function in Eq. (36a) reads as in (see Appendix C):

$$\mathscr{E}_P^{(RW)}\left(\vec{\tilde{X}}\right) = \gamma_1\exp\left(\tilde{T}_P\right)+\gamma_1\gamma_2(2\pi)^2\exp\left(2\tilde{R}\ -\ \tilde{T}_P\right)+\gamma_3(2\pi)^3 \times\exp\left(3\tilde{R}\ -\ 2\tilde{T}_P\right)+\gamma_4\exp\left(\tilde{z}\ +\ \tilde{T}_P\ -\ \tilde{y}\right); \quad (37)$$

and,

(ii) by definition, c_0 in Eq. (36b) reads as in:

$$c_0 \triangleq 1+\left(2\ v^{(MAX)^2}\Big/\ \gamma_5\ z^{(MIN)^2}\right), \quad (38a)$$

with the positive constant: $z^{(MIN)}$ given by (see Appendix C):

$$z^{(MIN)} \triangleq \min_{\substack{0\le T_P\le T_P^{(MAX)}\\ 0\le v\le v^{(MAX)}}} z \overset{(a)}{=} \min_{\substack{0\le T_P\le T_P^{(MAX)}\\ 0\le v\le v^{(MAX)}}}\left(\left(1+\left(\frac{2\pi}{T_P}\right)^2\frac{v^2}{g^2}+\frac{v^4}{{\gamma_5}^2}\right)^{\frac{1}{2}}-\frac{v^2}{\gamma_5}\right)^{\frac{1}{2}}, \quad (38b)$$

where (a) follows from the definition in Eq. (C.2).

Regarding the reported P2 optimization problem, two main remarks are in order. First, the l.h.s. of Eq. (38a) involves only the (a priori known) system parameter γ_5. Therefore, the corresponding minimum may be numerically pre-evaluated off-line through a grid search over the allowed domain: $\left[0,\ v^{(MAX)}\right]\times\left[0,\ T_P^{(MAX)}\right]$.

Second, thanks to the convexification procedure developed in Appendix C, the objective function in Eq. (37) is in posynomial (and convex [47]) form. Since all the involved constraints are posynomial functions, we conclude that the P2 optimization problem is, by definition, an instance of GP [47].

5.1. Designed primal-dual iterations for problem solving

Slater's qualification conditions for convex optimization problems require that there exists at least a feasible point that meets all the involved convex constraints with the strict inequalities [47]. Since this is guaranteed when all the sufficient feasibility conditions of the problem are strictly met [47], hereafter we assume that the sufficient feasibility conditions in Eqs. (28), (31) and (34) are strictly satisfied, so that P1 and P2 meet the Slater's qualification conditions. As a consequence, the solution:

$$\vec{\tilde{X}}^* \triangleq \left[\tilde{R}^*\ \tilde{H}^*\ \tilde{T}_P^*\ \tilde{y}^*\ \tilde{z}^*\right]^T, \quad (39)$$

of P2 is the saddle-point of the corresponding Lagrangian function [47]. Since P2 is a convex optimization problem, the box constraints in Eqs. (36d), (36e) and (36f) may be managed as implicit ones. Hence, the resulting partial Lagrangian function of P2 reads as in:

$$\mathscr{L}\left(\vec{\tilde{X}},\vec{\mu}\right) = \mathscr{E}_P^{(RW)}\left(\vec{\tilde{X}}\right)+\sum_{i=1}^{6}\mu_i\ \varphi_i\left(\vec{\tilde{X}}\right), \quad (40)$$

where: $\mu_i \ge 0,\ i=1,\ldots,6$, is the nonnegative multiplier (measured in (J)) associated to the i-th convex constraint of P2, while: $\vec{\mu} \triangleq \left[\mu_1\ldots\mu_6\right]^T$ is the resulting six-dimensional nonnegative column vector. Furthermore, since strong-duality holds [47], the (unique) solution: $\left\{\vec{\tilde{X}}^*,\ \vec{\mu}^*\right\}$ of P2 is the saddle-point:

$$\max_{\vec{\mu}\ge\vec{0}}\left\{\min_{\vec{\tilde{X}}\in\mathscr{S}}\left\{\mathscr{L}\left(\vec{\tilde{X}},\vec{\mu}\right)\right\}\right\}, \quad (41)$$

of the Lagrangian function in Eq. (40) [47], where: $\mathscr{S}$ in Eq. (41) is the subset of $\mathbb{R}^5$ featured by the (implicit) box constraints in Eqs. (36d), (36e), and (36f). This is the orthogonal projection onto the feasible Cartesian-product set: $\mathscr{S}\times\ [0,\ \infty)^6$ of the solution of the following algebraic equation:

$$\vec{\nabla}\mathscr{L}\left(\vec{\tilde{X}},\vec{\mu}\right) = \vec{0}_{11\times1}, \quad (42)$$

where: $\vec{\nabla}\mathscr{L}(.)$ is the 11-dimensional gradient vector of $\mathscr{L}(.)$. This last one is carried out w.r.t. the primal and dual scalar variables that are gathered by the vectors $\vec{\tilde{X}}$ and $\vec{\mu}$ respectively. Since the objective function and the constraints of P2 are nonlinear, therefore the solution of the algebraic vector equation in Eq. (42) resists closed-form computation. Furthermore, even if it would be possible to solve it in closed-form under some specific (and simpler) cases, the obtained solution should be re-computed from scratch when the setting of the operating conditions of Fig. 1 changes. This may happen, for example, when the setting of the UAV flying parameters (like $v^{(MAX)}$, $H^{(MAX)}$ and/or $H^{(MIN)}$) changes, or the setup of the QoS target thresholds (like P_{SER} and/or TH_{PL}) varies.

However, primal-dual iterations may be implemented to numerically compute the solution of the algebraic equation system in Eq. (42). In fact, as pointed out in [47], the primal-dual algorithm is an iteration-based procedure that simultaneously updates on a per-step basis both

the primal: $\vec{\tilde{X}}$, and the dual: $\vec{\mu}$ variables of the underlying Lagrangian function in Eq. (40), in order to drive it toward its saddle-point of Eq. (41). Hence, after introducing the dummy position:

$$\left[\chi\right]_a^b \triangleq \max\left\{a; \min\left\{b;\ \chi\right\}\right\}, \tag{43}$$

the $(k+1)$-th updating of the l-th scalar component: $\tilde{x}_l$, $l = 1, \ldots, 5$, of the $\vec{\tilde{X}}$ vector reads as in [47]:

$$\tilde{x}_l^{(k+1)} = \left[\tilde{x}_l^{(k)} - g_{\tilde{x}_l}^{(k)}\ \partial_{\tilde{x}_l}\mathscr{L}\left(\vec{\tilde{X}}^{(k)}, \vec{\mu}^{(k)}\right)\right]_{\tilde{x}_l^{(MIN)}}^{\tilde{x}_l^{(MAX)}}, \quad k = 0,\ 1, \ldots, \tag{44}$$

while the corresponding updating of the i-th multiplier: μ_i, $i = 1, \ldots 6$, is given by:

$$\mu_i^{(k+1)} = \left[\mu_i^{(k)} + g_{\mu_i}^{(k)}\ \varphi_i\left(\vec{\tilde{X}}^{(k)}, \vec{\mu}^{(k)}\right)\right]_0^{\infty}, \quad k = 0,\ 1, \ldots, \tag{45}$$

where: (i) k is an integer-valued nonnegative iteration index; (ii) $\left\{g_{\tilde{x}_l}^{(k)},\ l = 1, \ldots, 5\ ;\ \ g_{\mu_i}^{(k)},\ i = 1, \ldots, 6\right\}$ is the set of (time-varying) nonnegative step-sizes, which may also depend on the variables to update; and, (iii) $\varphi_i(.)$ in Eq. (45) is the derivative of the Lagrangian function in Eq. (40) w.r.t. μ_i, $i = 1, \ldots, 6$.

Regarding the convergence of the reported primal-dual iterations, three main remarks are in order. First, under the strict feasibility, P2 admits at least a global minimum. Second, the objective function in Eq. (37) is strictly convex, therefore, P2 is also a strictly convex optimization problem and its global minimum is unique [47]. Third, the convergence of the primal-dual iterations to their (unique) global minimum is guaranteed, regardless of the (even infeasible) starting point: $\left\{\vec{\tilde{X}}^{(0)},\ \vec{\mu}^{(0)}\right\}$. We anticipate that, in the carried out simulations, we adopt:

$$\begin{aligned} &\tilde{R}^{(0)} = \log R^{(MAX)}\ ,\ \tilde{H}^{(0)} = \log H^{(MAX)}\ ,\ \tilde{T}_P^{(0)} = \log \tilde{T}_P^{(MAX)}\ , \\ &\tilde{y}^{(0)} = \tilde{z}^{(0)} = 0\ ,\ \text{and:}\ \ \mu_i = 0\ ,\ \ i = 1, \ldots, 6, \end{aligned} \tag{46}$$

as starting point of the implemented iterations.

In view of computational complexity, the main feature of the developed solving approach is that its implementation does *not* require multiple nested iteration loops, as it typically happens in the case of solving algorithms based on the so-called Successive Convex Approximation (SCA) approach [7,14]. As a consequence, the overall computational complexity required by the implementation of the iterations in Eqs. (44) and (45) scales up only in a *linear* way:

$$\mathscr{O}\left(11 \times\ I^{(MAX)}\right),$$

with the number $I^{(MAX)}$ of performed primal-dual updates, where the multiplying coefficient accounts for the number of (scalar) updates to perform at each iteration. The attained reduced implementation complexity is the main motivation behind the pursued convexification of the original non-convex problem in P1.

5.2. Proposed regularized adaptive step-size

In principle, further reduction of the computational complexity may be attained by suitably designing the step-sizes in Eqs. (44) and (45) to *reduce* as much as possible the number $I^{(MAX)}$ of needed iterations. Motivated by this consideration, we design a regularized and adaptive formula that applies to the computation of all step-sizes in Eqs. (44) and (45). We prove that the proposed step-size formula retains a number of appealing analytical properties, which may speed up the stable convergence of the implemented primal-dual iterations.

Specifically, after indicating by u a primal-dual scalar optimization variable, we compute its k-th step-size $g_u^{(k)}$ as follows:

$$g_u^{(k)} \equiv \frac{a_0}{\sqrt{a_1 + \left(\partial_u \mathscr{L}^{(k)}\right)^2}}\ , \quad k = 0,\ 1, \ldots, \tag{47}$$

where: $\partial_u \mathscr{L}^{(k)}$ is the (scalar) derivative of the Lagrangian function in Eq. (40) w.r.t. the (scalar) optimization variable u, while a_0 and a_1 are two positive regularizing hyper-parameters to be tuned by numerical trials. The main reason behind the design of Eq. (47) are the limit properties detailed in the Appendix D.

These properties point out that the main goal of the setting of the hyper-parameters a_0 and a_1 is to *regularize* the behaviors of the corresponding product: $(g_u \times \partial_u \mathscr{L})$ in the limit cases of vanishing and growing values of $\left|\partial_u \mathscr{L}\right|$. The numerical results reported in Section 7 confirm this expectation and most importantly support the conclusion that values of the maximum iteration number $I^{(MAX)}$ in Eq. (46) limited up to a *few of tens* suffice for the stable convergence of the primal-dual iterations in Eqs. (44) and (45).

6. Implementation aspects

The goal of this section is to give insight into two aspects concerning the actual implementation of the optimization algorithm of Section 5 and the overall supporting system of Fig. 1, namely:

(i) the optimized setting of the path-loss threshold of Eq. (21) as well as its sensitivity to both the target QoS requirements, the adopted communication technology, and the (possible) GUs' heterogeneity; and
(ii) the main functional blocks of a Software Defined Networking (SDN)-aided virtualized (container-based) architecture that allows the GUs of Fig. 1 to share the communication-plus-computing infrastructure resources available at both the GCS and serving UAV.

6.1. Setting of the path-loss threshold and impact of GUs heterogeneity

By referring to Fig. 1, we consider the uplink communication from $GU\#K$ to the serving UAV. Hence, after denoting by: $\overline{\mathscr{P}}_{TX}(K)$ the average power (measured in (W)) transmitted by $GU\#K$, the corresponding minimum average power: $\overline{\mathscr{P}}_{RX}^{(MIN)}(K)$ received at the UAV is (see Eq. (9)): $\overline{\mathscr{P}}_{RX}^{(MIN)}(K) = \overline{\mathscr{P}}_{TX}(K)/\overline{L}^{(MAX)}$. Hence, the resulting minimum Signal-to-Noise-plus-Interference Ratio ($SINR$) experienced by $GU\#K$ reads as in:

$$\begin{aligned} SINR_K^{(MIN)} &\triangleq \overline{\mathscr{P}}_{RX}^{(MIN)}(K) \Big/ \left(\overline{\mathscr{P}}_N(K) + \varrho\ \overline{\mathscr{P}}_I^{(MAX)}(K)\right) \\ &= \overline{\mathscr{P}}_{TX}(K) \Big/ \left(\overline{L}^{(MAX)}\left(\overline{\mathscr{P}}_N(K) +\ \varrho\ \overline{\mathscr{P}}_I^{(MAX)}(K)\right)\right), \end{aligned} \tag{48}$$

where: (i) $\overline{\mathscr{P}}_N(K)$ is the average noise power suffered by $GU\#K$; (ii) $\overline{\mathscr{P}}_I^{(MAX)}(K)$ is the maximum average multiple-access interference power possibly caused by the concurrent transmissions of other GUs; and, (iii) ϱ, with $0 \le \varrho\ \ \le 1$, is the interference cancellation factor [33]. Since this last depends on the used MAC technology, it vanishes when Orthogonal Multiple Access (OMA) techniques (as, for example, O-FDMA or O-TDMA) are employed in Fig. 1, while it typically falls in the open interval: $(0, 1)$ in the case of utilization of NOMA techniques [25,33]. Since OMA (resp., NOMA) techniques are energy (resp., bandwidth) efficient but bandwidth (resp., energy) wasting, the actual value of ϱ is typically set so to trade-off energy-vs.-bandwidth usage [26,33].

After setting ϱ, the minimum value (in linear scale): $TH_{SINR}(K)$ allowed the $SINR_K^{(MIN)}$ depends on both the required QoS parameters (like the minimum bit-rate at the Physical Layer and/or the minimum throughput at the MAC Layer required by $GU\#K$), as well as the adopted technology for supporting the $GU\#K$-UAV communication link. Just as an application example of practical interest, Table 1 from

Table 1
SINR thresholds, Physical transmission rates and related MAC throughput under the *IEEE* 802.11a communication technology. Case of single receive antenna.

TH_{SINR} (dB)	*Physical Bit-Rate* (Mb/s)	*MAC Throughput* (Mb/s)
25.0	54.0	32.5
18.0	36.0	24.6
11.0	18.0	14.4
9.0	12.0	10.2
8.0	9.0	7.8
6.0	6.0	5.4

[14] reports the needed SINR thresholds (in (dB)) for enabling various bit-rate/throughput requirements in the (quite common) case in which the $GU\#K$-UAV link is supported by the WiFi *IEEE* 802.11a technology.

Hence, in order to account for the (possible) GUs heterogeneity, let: $BR(K)$ (measured in (b/s)) and: $\eta_B(K)$ (measured in $\left(\frac{\text{b}}{\text{s}\times\text{Hz}}\right)$) be the target (e.g., desired) average bit-rate and the spectral efficiency of the coded modulation transceiver equipping $GU\#K$, respectively. Then, since the resulting communication bandwidth: $BW(K)$ (measured in (Hz)) equates to the ratio:

$$BW(K) = \frac{BR(K)}{\eta_B(K)}\,, \tag{49a}$$

the (previously introduced) noise and interference powers experienced by the $GU\#K$-UAV link read as in:

$$\overline{\mathscr{P}}_N(K) = \overline{\mathscr{N}}_0(K) \times BW(K), \text{and: } \overline{\mathscr{P}}_I^{(MAX)}(K) = \overline{\mathscr{N}}_I^{(MAX)} \times BW(K), \tag{49b}$$

where: $\overline{\mathscr{N}}_0(K)$ and $\overline{\mathscr{N}}_I^{(MAX)}(K)$ are the corresponding average noise and interference power density spectra (measured in (W/Hz)). Finally, after introducing the relationships in Eq. (49a) into the SINR expression in Eq. (48), and, then, imposing the set of per-GU constraints: $\text{SINR}_K^{(MIN)} \geq TH_{SINR}(K), \forall K$, on the minimum required SINR values,[5] we conclude that the threshold: TH_{PL} on the maximum allowed average path-loss in Eq. (21) should equate to the following minimum:

$$\begin{aligned} TH_{PL} &= \min_K \left\{ \frac{\overline{\mathscr{P}}_{TX}(K)}{TH_{SINR}(K) \times BW(K) \times \left(\overline{\mathscr{N}}_0(K) + \varrho \overline{\mathscr{N}}_I^{(MAX)}(K)\right)} \right\} \\ &\equiv \min_K \left\{ \frac{\overline{\mathscr{P}}_{TX}(K) \times \eta_B(K)}{TH_{SINR}(K) \times BR(K) \times \left(\overline{\mathscr{N}}_0(K) + \varrho \overline{\mathscr{N}}_I^{(MAX)}(K)\right)} \right\}. \end{aligned} \tag{50}$$

The above relationship: (i) accounts for the (possible) GUs' heterogeneity in terms of transmit powers, required bit-rates, demanded bandwidths and experienced noise and/or interference powers; and, (ii) when it is combined to the constraint in Eq. (21) on the maximum tolerated path-loss, guarantees network stability, that is, it allows each $GU\#K$ to attain his average target bit-rate $BR(K)$.

Passing to consider now the more general case in which the serving UAV is equipped with $N_{RX} \geq 2$ multiple receive antennas, we note that the typical UAV-aided operative environments tend to be, for the most part, LoS-dominated [49], so that achieving diversity receive gain by exploiting multipath fading is challenging [50,51]. However, multiple receive antennas could still provide array gains, because receiving antenna arrays may be used for decreasing the experienced path loss, as well as to mitigate the (possibly present) multiple-access interference [10,52]. In this regard, the analysis carried out in [49] supports the conclusion that, at least when: (i) the receive UAV is equipped with a linear array of N_{RX} antennas that are suitably spaced apart; and (ii) the antenna outputs are mixed by a Maximal Ratio Combining (MRC) receiver, then the resulting path-loss threshold: $TH_{PL}(N_{RX})$ scales up with N_{RX} in a (near) linear way, that is,

$$TH_{PL}(N_{RX}) \cong N_{RX} \times TH_{PL}\,, \tag{51}$$

with TH_{PL} still given by Eq. (50).

Finally, we point out that the performed link-analysis still apply verbatim to the dual case of UAV-to-GU communication, at least when channel reciprocity holds. Typically, this is the case in which Time Division (TD) is used in Fig. 1 as duplexing technique [10,52].

6.2. Proposed virtualized supporting system architecture

In the last years, network-supported computing applications are progressively shifting from monolithic services to graph-based ones with multiple single-purpose and loosely-coupled microservices. This shift has been already experienced in the cloud providers' realm (e.g., Amazon, Twitter and Netflix, to name a few, have already adopted the microservice model) and it is becoming pervasive in the Edge/Fog realm. According to this consideration, the goal of this section is to design the main building blocks of the UAV and GCS functional architectures for the support of the developed trajectory optimization algorithm, as well as the related orchestartion of the computing-plus-communication resources hosted by the GCS, serving UAV and served GUs. The proposed architectures rely on the combined SDN/NFV paradigm envisioned for the next 6G-aided networked microservice-based computing/communication systems [40,48]. According to this emerging paradigm, the serving UAV is viewed as distributed and programmable networked computing platform, which is capable of executing microservices in the form of chained Virtual Functions (VSs) in response to the (time-varying) service demands of the GUs and/or UAV operator. By doing so, the UAV can be dynamically and quickly deployed for supporting different missions, which may require the simultaneous provisioning of heterogeneous computing-communication microservices, as well as microservice migration [53].

Overview of the supporting aerial-terrestrial infrastructure According to this vision, as, for example, in [2,7,10], the battery-powered UAV of Fig. 1 is assumed to be equipped with a flight management system i.e., Local Controller (LC), a propulsion system, a battery bank, a communication module, and a miniaturized computing module. The Hard-Ware (HW) communication equipment hosted by the UAV embraces (at least) two wireless transceivers, which typically operate over non-overlapped frequency bands. Specifically, a first transceiver is used for allowing the UAV to communicate with the GCS of Fig. 1, while the second one is employed for communicating with the served GUs. Both transceivers may convey bi-directional data and control flows. The UAV-GCS control path is used by: (i) the UAV, in order to send to the GCS a number of UAV and/or GU parameters, like, UAV coordinates, flying speed, residual

[5] Just as an example, let us assume that $GU\#K$ requires a bit-rate: $BR(K)$ of 18×10^6(b/s). Hence, directly from the second column of Table 1, we have that the corresponding SINR threshold: $TH_{SINR}(K)$ (in linear scale) is: $10^{0.1\times11} \cong 12.59$.

battery level, link states, number of served GUs and their communication/computing requirements; and (ii) the GCS, to send to the UAV a number of commands regarding, for example, the optimized trajectory parameters as well as the dynamically scheduled per-user allocation of the available UAV communication-plus-computing resources (per-GU bandwidth, communication power, computing frequency and storage capacity). The UAV-GCS data path is used as data backhaul to allow the served GUs to send/receive data to/from the remote Internet by using the UAV (resp., GCS) as an aerial (resp., terrestrial) Internet Gate-Way (GW).

A glimpse of the ETSI virtualization standard To address the open challenges previously listed in Section 2, and assure the convergence of the proposed architecture with standardized frameworks, we develop a proposal that is compliant with the SDN-NFV reference architecture recommended by the European Telecommunication Standards Institution (ETSI) [40,48]. ETSI standardized a management and orchestration framework as well as a suite of functional building blocks and the related reference points, i.e. the inter-block communication interfaces. According to this standard, we mention that [40]:

(i) the task of a Virtual Network Function (VNF) is to emulate in Software (SW) the functionality of a specific network device or computing node. The ordered interconnection of multiple VNFs gives rise to a Micro-Service (MS);
(i) task of the NFV Infrastructure (NFVI) is to provide the physical resources that are required for the deployment, execution and management of the instantiated MSs. These resources are dynamically allocated to each VNF by a Virtualization Layer (typically, a Hypervisor or a Container Engine), whose main goal is to decouple the VNF software from the underlying execution hardware; and
(ii) the main task of the Manager and Orchestrator (MANO) block is to plan and support the coordinated execution of all microservices implemented by the instantiated VNFs [40]. To this end, the MANO relies on the support of the Virtual Infrastructure Manager (VIM), VNF Manager (VNFM) and NFV Orchestrator (NFVO), whose specific tasks are the control of the physical resources of the NFVI, the management of the life cycle of the VNFs and the coordination of the actions of the running VNFs respectively. For these purposes, the VIM may be also equipped with an SDN Controller [40], as well as being capable of sustaining service migration [53].

The proposed virtualized supporting architecture In agreement with the (shortly reviewed) ETSI standard, the main functional blocks of the proposed SDN/NFV-based architecture at the GCS (resp., at the serving UAV) is reported in Fig. 3 (resp., Figs. 4 and 5).

1) The proposed GCS architecture In our proposal, the overall system of Fig. 1 is centrally managed by the GCS, whose main tasks are to: (i) plan the flying trajectories of (possibly, multiple) serving UAVs on the basis of the requirements of the UAV operators and served GUs; (ii) deploy the needed VNFs on the serving UAV(s) and program the corresponding network switches; (iii) monitor the GU requirements to dynamically reconfigure the corresponding UAV resources; and (iv) allow the served GUs to access the remote Internet by using the flying UAV(s) as intermediate switch(es).

To support this last communication task, the GCS architecture of Fig. 3 is assumed to be equipped with a *Central Internet GW* and a *Central UAV GW* to implement the communication paths to the remote Internet and the serving UAV(s) respectively. Furthermore, since in our framework, the served GUs have only *indirect access* to the remote Internet (they may access the remote Internet by using only the UAVs as intermediate switching units), the *Central MUX-DeMUX* of Fig. 3 performs mu-demultiplexing of the data flows that must be forwarded to (resp., are received from) the served GUs.

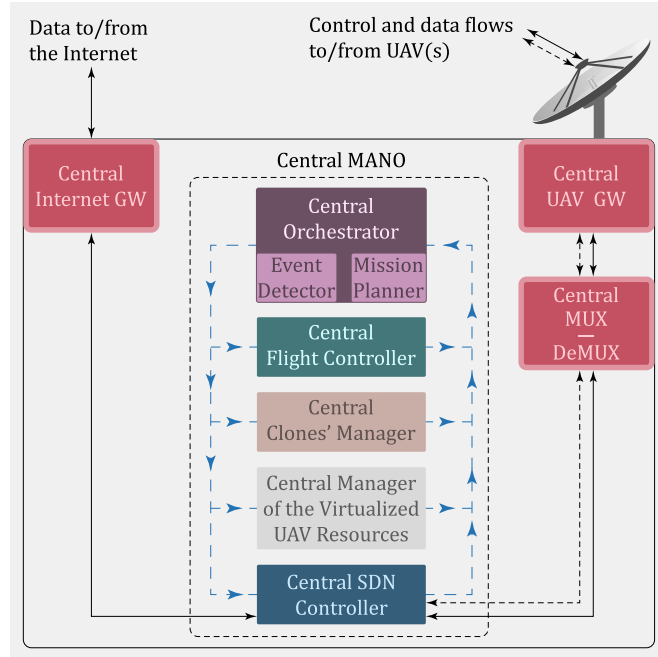

Fig. 3. The designed SDN/NFV-supported GCS architecture. Continuous lines: = data flows; Dashed lines: = control flows; *MANO*: = MANager and Orchestrator; *MUX*: = MUltipleXer; *SDN*: = Software Defined Networking; *GW*: = GateWay.

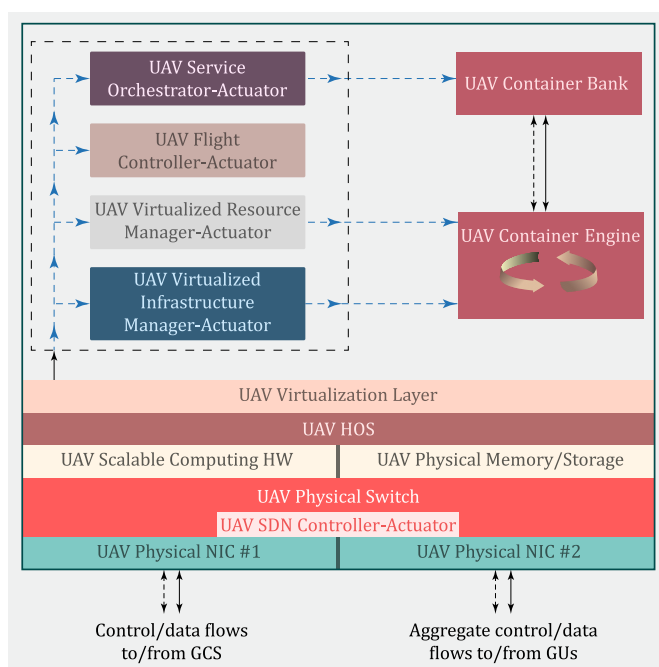

Fig. 4. The designed virtualized functional architecture at the UAV. Continuous lines: = data flows; Dashed lines: = control flows; *MANO*: = MANager and Orchestrator; *NIC*: = Network Interface Card; *HOS*: = Host Operating System; *HW*: = Hard-Ware; *SDN*: = Software Defined Networking.

The main goal of the *Central MANO* of Fig. 3 is the management and orchestration of the UAV trajectory and available infrastructure resources as well as the deployment and chaining of the VNFs to be instantiated. Being the "brain" that hosts the system intelligence, in our proposal, the Central MANO is composed of the following main intercommunicating functional blocks (see the dashed box of Fig. 3):

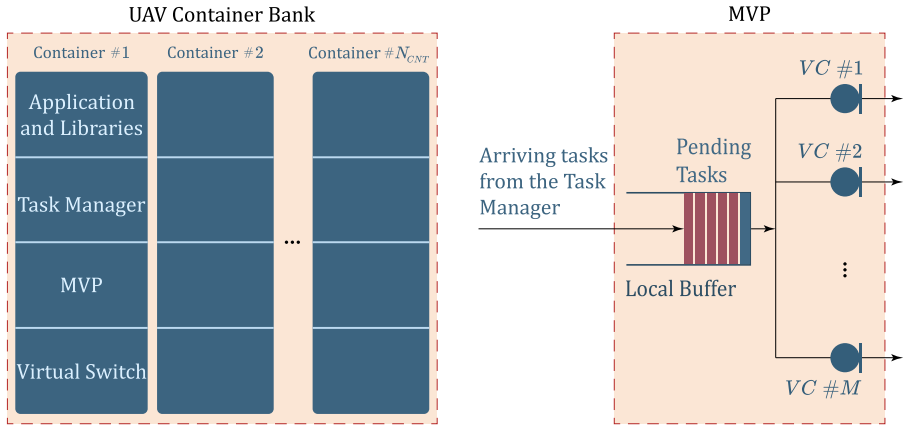

Fig. 5. The designed container-based architecture for the implementation of the GU clones at the serving UAV. *(a)* Container environment; *(b)* Functional architecture of a multi-core virtual processor. *MVP*:= Multi-core Virtual Processor; *VC*:= Virtual Core; N_{CNT}:= Number of CNTainers; M:= Number of per-container virtual cores.

(i) the *Central Orchestrator*, whose twofold main tasks are to: (a) plan the UAV mission on the basis of the mission descriptors provided by the UAV operator; and (b) monitor the system state on a periodic (or even event-driven) basis to quickly detect anomalies (link failures, resource depletions, and mechanical failures) and/or stressing phenomena (link congestions, deep fading phenomena, and energy breakdown);
(ii) the *Central Flight Controller*, which implements the primal-dual iterations of Eqs. (44) and (45) for the optimized setting of the UAV trajectory parameters;
(iii) the *Central Clones' Manager*, which is the unit responsible for specifying the descriptors of the microservices to be provided to the GUs, with each microservice being an ordered composition of specified VNFs;
(iv) the *Central Manager of the virtualized UAV resources*, whose main goals are to configure the working parameters of each VNF and plan the related policies for the allocation of the available HW/SW resources to the instantiated VNFs; and
(v) the *Central SDN Controller*, which configures the physical switches equipping the serving UAV(s) to establish a suitable set of control and data communication paths toward the served GUs and the remote Internet (see the dashed and continuous paths of Figs. 3 and 4). For this purpose, the Central SDN Controller may utilize southbound APIs based on the OpenFlow protocol [40,48].

2) The proposed virtualized UAV architecture Fig. 4 reports the proposed layered architecture at the serving UAV.

At the bottom of the designed architecture, there are the networking (switches and related SDN local controller), computing (processing units) and storage (physical memory) resources that equip the UAV. These resources are managed by a *Host Operating System (HOS)* and they are presented in abstract (hardware-independent) form to the higher layers of Fig. 4 by the UAV Virtualization Layer, (typically, a Hypervisor [40]).

The blocks embraced by the *Local UAV MANO* (see the dashed box of Fig. 4) mirror the corresponding ones at the Central MANO of Fig. 3. There are two main reasons for this architectural choice. Specifically, when the GCS of Fig. 1 is present, each block of the Local UAV MANO in Fig. 4 acts as (mere) *local actuator* of the global decisions taken by the corresponding block at the Central MANO of Fig. 3. However, when the GCS is absent or temporarily failing, the *Local UAV MANO* may exploit its *local* intelligence for managing the *local* resources of the hosting UAV. In this last case, the UAV *Flight Controller* of Fig. 4 becomes responsible to implement the iterations of Eqs. (44) and (45) for the computation of the optimized trajectory parameters.

The *Container Engine* of Fig. 4 acts as local VIM, where its main task is to implement the scheduling policy dictated by the Central MANO to assign (on a round-robin basis) the locally available UAV physical resources to the sustained bank of running containers. Depending on both the resource assignment performed by the Container Engine and the required service, each served GU may be associated to one or more UAV-hosted containers, while each container may execute one or more VNFs.

For this purpose, in our proposal, the functional architecture of each container is organized as in Fig. 5a.

This architecture embraces:

(i) *Application codes and Libraries* for the SW implementation of the executed VNFs;
(ii) a *Task Manager*, which is responsible of the ordered execution of the (multiple and inter-dependent) tasks that compose each executed VNF;
(iii) *a Multi-core Virtual Processor (MVP)*, whose architecture is sketched in Fig. 5b. It exploits a bank of Virtual Cores (VCs) for the parallel execution of the sequence of tasks provided by the Task Manager; and
(iv) a *Virtual Switch*, which allows both inter-container communication as well as container-to-Container Engine communication. The virtual switches hosted by the UAV may be locally managed by the corresponding Local SDN Controller of Fig. 4, while (if required) inter-UAV communication is managed by the corresponding Central SDN Controller of Fig. 3. Inter-container communication may rely on service migration protocols [53].

3) How the overall joint UAV-GCS architecture works The task of the control and data communication paths of Figs. 3 and 4 is to convey control messages, Internet data, and offloaded computing data. In this regard, we observe that, although the control plane of our overall architecture is centralized at the GCS, the corresponding data plane may remain *still* distributed. This is because, according to [5] and the references therein, each GU may be equipped with (limited) computing resources so that it may locally process a part of his overall workload, while offloading to the serving UAV(s) the remaining one. However, in our setup, the GU access to the remote Internet is undirected so that all the data to/from the Internet must transit through the GCS gateways (see Fig. 3). As a consequence, in our proposal, the communication paths for data offloading are single-hop, but the corresponding control and Internet communication paths span (at least) two hops, with a hop that is sustained by the wireless backhaul of Fig. 1.

Table 2
Environmental parameters of the simulated logistic LoS probability model [19].

Environment	B	C (deg)	η_{LoS} (dB)	η_{NLoS} (dB)
Sub-Urban (SU)	4.88	0.43	0.1	21
Urban (UB)	9.61	0.16	1.0	20
Dense Urban (DU)	12.08	0.11	1.6	23
High rise Urban (HU)	27.23	0.08	2.3	34

By exploiting the established control paths, the *Event Detector* at the Central MANO of Fig. 3 periodically acquires information about the UAV state(s), link states as well as contextual information about the computing/communication profiles and service requirements of the served GUs. This information is gathered by the serving UAV(s), relayed to the GCS and then stored into three main tables, namely the GU table, UAV routing table, and UAV service table. Specifically, The GU table may include information on, for example, the per-GU residual battery capacities and per-GU available CPU cycles. The routing (resp., UAV) table may store per-link loads and routing paths (resp., per-UAV computation loads and residual UAV battery capacity), while the service table may store per-VNF computational-communication loads as well as per-service descriptors and related per-service QoS requirements.

Overall, under the proposed architecture framework, the process of service handling proceeds as follows. The requiring GU forwards its service request to the GCS via the (nearest) serving UAV. When the Central MANO of Fig. 3 receives the GU service request message, it updates all its information tables and performs service access control. In the case that the GU request is accepted, the Central MANO plans the corresponding service offloading strategy and resource allocation strategy in agreement with the QoS targets requested by the GU. During this phase, instantiation of new VNFs and/or re-scaling of already instantiated VNFs may take place. Finally, the accepted GU service request enters the execution phase.

7. Numerical tests and performance comparisons

The numerical tests have been carried out on a PC equipped with: (i) an AMD Ryzen 9 5900X 64-Core 3.7 GHz processor; (ii) a GeForce RTX 3080 graphics card; and (iii) 256 GB RAM. The utilized SW platform has been MATLAB R2022b.

The default LoS probability model used for the tests is the (quite usual) logistic. It reads as in [19]:

$$P_{LoS}(\theta) = 1 \Big/ \left[1 + C\exp\left(-B\left(\theta - C\right)\right)\right], \quad 0 \le \theta \le 90, \tag{52}$$

where the (numerically evaluated) environment-dependent values of the B and C fitting parameters are reported in Table 2.

Furthermore, unless otherwise stated, the simulated settings of the gamma parameters of the propulsion power model of Eq. (11) are as in [54] (see Table A.10 in Appendix A).

7.1. Performance tests

The goal of a first set of numerical tests is to compare the dynamic behaviors of the optimized energy traces and associated Lagrange multipliers when the primal dual-iterations of Eqs. (44) and (45) are carried out under the proposed adaptive step-size of Eq. (47) (see Figs. 6a and 6c) and the fixed step-size, e.g., $g_u^{(k)}$ in Eq. (47) is statically set to a_0 (see the Figs. 6b and 6d).

A comparative view of the set of plots of Fig. 6 shows that a number $I^{(MAX)}$ of iterations around 20 suffices for the convergence of the energy and multiplier traces under the adaptive step-size of Eq. (47). However, about $I_{FSS}^{(MAX)} = 200$ iterations are needed when the primal-dual iterations of Eqs. (44) and (45) are implemented under the fixed step-size.

This conclusion is, indeed, further corroborated by the plots of Fig. 7.

They refer to a quite challenging time-varying scenario, in which the tolerated path-loss threshold TH_{PL} in Eq. (19) changes in an abrupt and unpredictable way at the iteration indexes: 1, 25, 50, and 75 (resp., 1, 250, 500, and 750) under the adaptive (resp., fixed) step-size setting by following the step-wise path: TH_{PL}: 160 (dB) → 155 (dB) → 165 (dB) → 160 (dB). After each change of the path-loss threshold, the optimal trajectory parameters are computed by running the primal-dual iterations of Eqs. (44) and (45) under three adaptive (see Fig. 7a) and fixed (see Fig. 7b) step-size settings to re-optimize the corresponding propulsion energy.

A comparative examination of the plots of Fig. 7 leads to two main insights. First, it is confirmed that the convergence speed under the proposed adaptive step-size is around a factor 10× larger than the one experienced under the corresponding fixed step-size. This is due to the (previously stressed) asymptotic properties of the adaptive step-size relationship of Eq. (47), which allow us to use values for the regularizing parameter a_0 as high as 0.15 without suffering too much from instability phenomena. On the contrary, the maximum feasible value of a_0 is of the order of: 5.0×10^{-6} under the fixed step-size setting and this is the reason for the slow (although admittedly smooth) convergence exhibited by the plots of Fig. 7b. Second, under the adaptive step-size setting, values of a_0 (resp., a_1) in Eq. (47) falling in the (quite large) interval: 0.05 - 0.15 (resp., 0.1 - 2.5) seem to guarantee good trade-offs among the contrasting requirements of quick reaction to environmental changes and stable behavior in the steady-state. Hence, unless otherwise stated, we adopt the setting: $a_0 = 0.1$, $a_1 = 1.5$, $I^{(MAX)} = 25$ in the execution of the primal-dual iterations of Eqs. (44) and (45) with adaptive step-size.

Performance sensitivity on the target out-of-service probability The numerical results of Table 3 aim to give insights about the joint sensitivity of the solution returned by the proposed optimization framework of Section 5 on the allowed out-of-service-probability: $P_{OUT} \equiv 1 - P_{SER}$ under the four environments of Table 2.

In this regard, a comparative examination of the entries of Table 3 leads to the following main insights about the obtained optimized solutions:

(i) the optimal values of the RW-UAV altitude H decreases (or, at least, does not increase) for decreasing P_{OUT} values. Intuitively, this is due to the fact that, when the target QoS requirements increase, the system reacts by decreasing the maximum GU-UAV distance $d^{(MAX)}$ in Eq. (8) to decrease the experienced path-loss;
(ii) the optimal values of the RW-UAV trajectory radius R increases (or, at least, does not decrease) for decreasing P_{OUT} values, in order to provide better coverage to the border GUs. At the same time, the optimal RW-UAV speed v tends to increase, in order to compensate the radius increments and attempt to stabilize the corresponding T_P values; and finally,
(iii) the resulting optimized values of the RW-UAV propulsion energy $\mathscr{E}_P$ increase for decreasing P_{OUT} values, i.e. larger QoS levels are paid through larger energy consumption. At the same time, as it could be expected, the optimized $\mathscr{E}_P$ decreases (or, at least, does not increase) by passing from the (more challenging) High rise Urban environment to the (less challenging) Sub-Urban one.

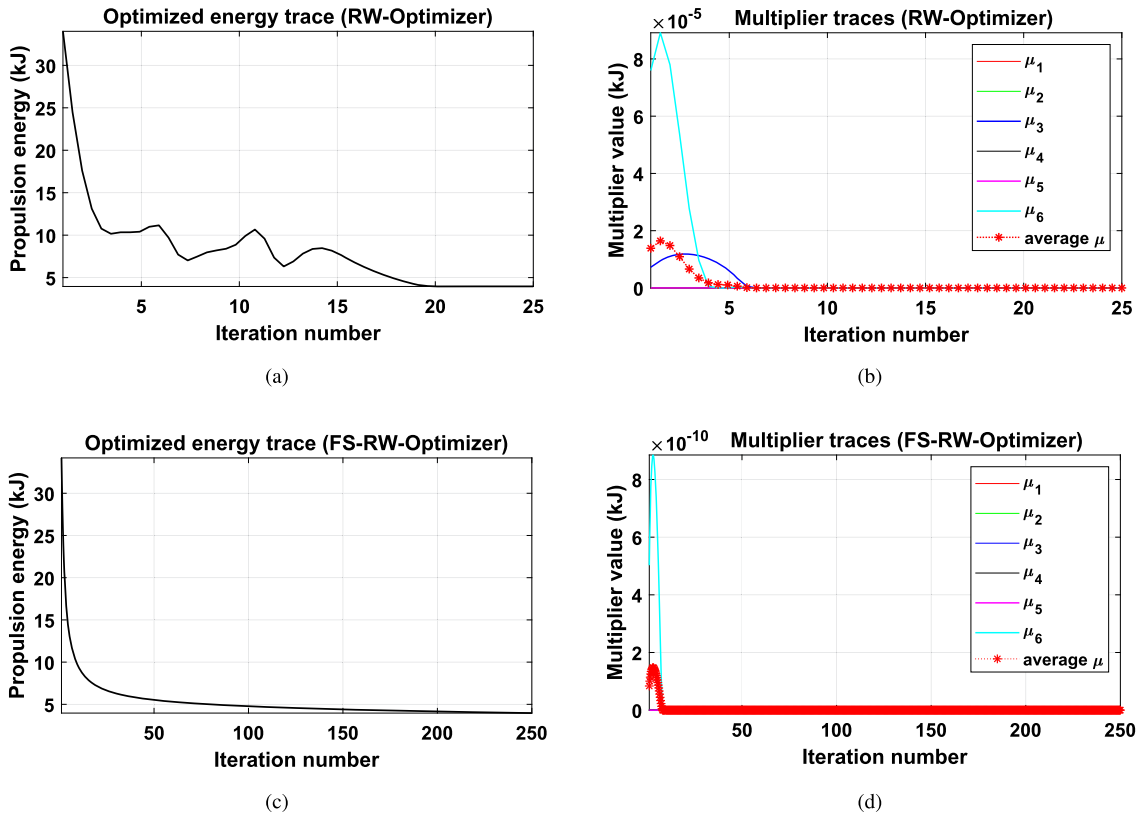

Fig. 6. Dynamic behaviors of the optimized energy traces and associated Lagrange multipliers (in (kJ)) of the simulated RW-UAV under adaptive and fixed step-sizes at $TH_{PL} = 155$ (dB). Case of the logistic LoS probability model under the High rise Urban environment at $P_{OUT} = 0.2$. *(a)* Energy trace under the adaptive step-size at $(a_0,\ a_1) = (0.05,\ 1.5)$; *(b)* Energy trace under the fixed step-sizes at $a_0 = 1.0 \times 10^{-6}$; *(c)* Traces of the Lagrange multipliers and associated average multiplier under the adaptive step-size at $(a_0,\ a_1) = (0.05,\ 1.5)$; and, *(d)* Traces of the Lagrange multipliers and associated average multiplier under the fixed step-size at $a_0 = 1.0 \times 10^{-6}$.

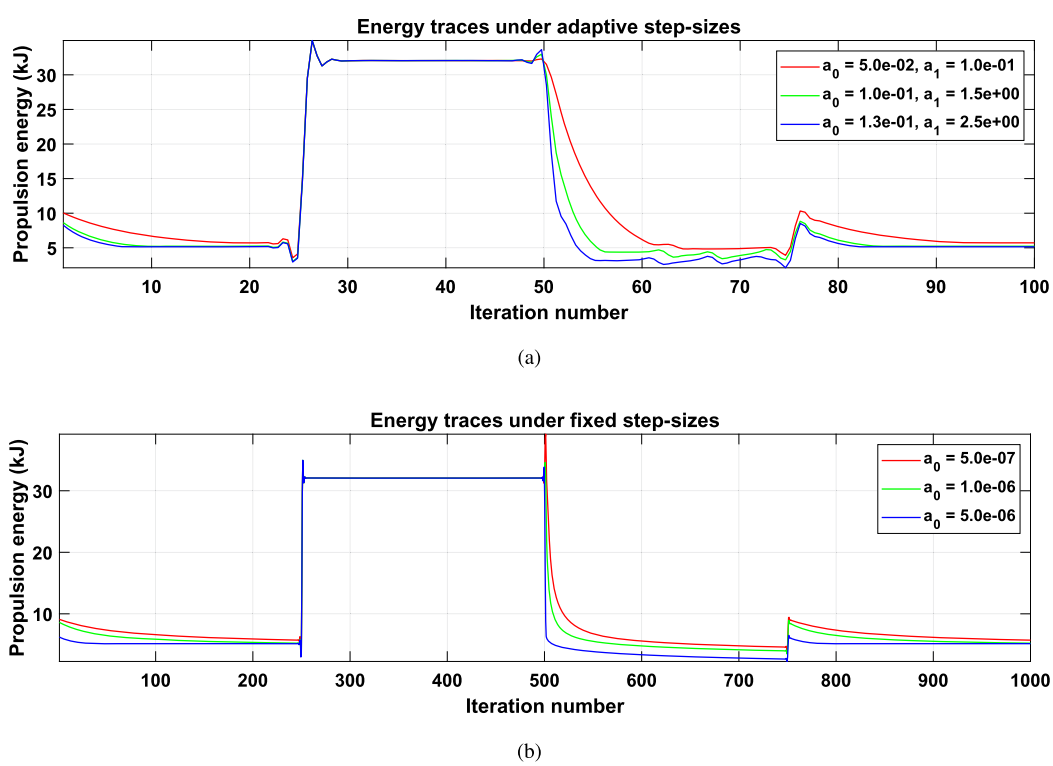

Fig. 7. Dynamic behaviors of the UAV energy traces at $P_{OUT} = 0.2$ under: *(a)* the proposed adaptive step-size at: $(a_0,\ a_1) = (0.05,\ 0.1)$, $(0.1,\ 1.5)$, $(0.15,\ 2.5)$; and, *(b)* the fixed step-size at $a_0 = 5.0 \times 10^{-7},\ 1.0 \times 10^{-6}\ ,\ 5.0 \times 10^{-6}$. Case of logistic LoS probability model under the High rise Urban environment.

Table 3
Performance sensitivity on P_{OUT} under the logistic LoS probability model at $TH_{PL} = 155$ (dB). *(a)* Sub-Urban environment; *(b)* Urban environment; *(c)* Dense Urban environment; *(d)* High rise Urban environment.

(a)

P_{OUT}	R (m)	H (m)	v (m/s)	$\mathscr{E}_P$ (J)
1.0×10^{-4}	7.18	34.62	11.91	3249.7
1.0×10^{-3}	6.86	62.08	11.57	3205.2
1.0×10^{-2}	4.80	350.00	8.99	2891.7
1.0×10^{-1}	2.11	350.00	4.91	2399.1
2.0×10^{-1}	1.04	350.00	2.94	2137.0

(b)

P_{OUT}	R (m)	H (m)	v (m/s)	$\mathscr{E}_P$ (J)
1.0×10^{-4}	9.47	62.08	14.21	3536.8
1.0×10^{-3}	9.18	102.21	14.14	3518.1
1.0×10^{-2}	8.49	102.21	13.30	3428.2
1.0×10^{-1}	3.31	350.00	6.92	2629.0
2.0×10^{-1}	2.36	350.00	5.44	2436.6

(c)

P_{OUT}	R (m)	H (m)	v (m/s)	$\mathscr{E}_P$ (J)
1.0×10^{-4}	9.31	242.83	14.42	3555.1
1.0×10^{-3}	9.22	236.79	14.20	3525.7
1.0×10^{-2}	8.79	350.00	13.66	3467.5
1.0×10^{-1}	7.23	350.00	12.00	3256.2
2.0×10^{-1}	5.99	350.00	10.52	3077.1

(d)

P_{OUT}	R (m)	H (m)	v (m/s)	$\mathscr{E}_P$ (J)
1.0×10^{-4}	9.53	134.62	14.49	3563.1
1.0×10^{-3}	9.31	249.27	14.11	3534.1
1.0×10^{-2}	8.79	259.27	13.66	3476.5
1.0×10^{-1}	8.27	350.00	13.17	3398.2
2.0×10^{-1}	7.22	350.00	11.99	3254.7

Joint performance sensitivity on the environmental parameters and path-loss threshold A comparative examination of the entries of Table 4c allows us to acquire the following two main insights about the combined impact of the setting of the path-loss threshold and the environmental parameters on the attained optimized RW-UAV performance:

(i) at fixed target path-loss threshold TH_{PL}, the resulting optimized energy consumption $\mathscr{E}_P$ increases by passing from the (gentle) Sub-Urban environment to the (challenging) High-rise Urban one. At the same time, under the same scenario, $\mathscr{E}_P$ decreases for increasing values of TH_{PL}; and
(ii) under a fixed environment, the optimized altitude values decrease (or, at least, do not increase) for decreasing TH_{PL} values to attempt to lower the worst-case experienced path-loss by decreasing the maximal distance: $d^{(MAX)}$ in Eq. (8).

Performance sensitivity on the adopted LoS probability model In the (quite recent) contribution [21], the following generalized logistic LoS probability model:

$$P_{LoS}(\theta) = \left(1 - B_4\right) + \frac{B_4}{1 + \exp\left(-(B_1 + B_2\theta)\right)}, \quad 0 \leq \theta \leq 90, \tag{53}$$

is proposed, in order to attain a better fitting against actual LoS probability measurements. Fig. 8 reports the plot of the logistic model of Eq. (52) against the corresponding one of Eq. (53) under the Urban environment (see Table A.10 in Appendix A for the corresponding setting of the B's parameters of Eq. (53) [21]).

The most evident feature of the plots of Fig. 8 is that they present two crossing points at θ values around 0.025 (deg) and 21 (deg). This does challenging to forecast the impact of these different LoS probability models on the performance returned by the optimization framework of Section 4. Hence, to give insight into this point, we have run the primal-dual iterations of Eqs. (44) and (45) under the generalized logistic model of Eq. (53). The obtained optimized results are reported in Table 5. They refer to under the Urban environment at $TH_{PL} = 155$ (dB).

A comparison of the entries of Table 5 with the corresponding ones of Table 3b leads to the following two main insights about the performance sensitivity of the developed optimization framework:

(i) the optimized energy consumption under the generalized logistic model is less than the corresponding ones under the logistic model. This provides (implicit) support to the conclusion that, in the simulated settings, the optimized values of $\theta^{(MIN)}$ in Eq. (8) mainly fall into the interval of Fig. 8, over which the generalized logistic model dominates the logistic one; and
(ii) both the optimized trajectory radii and RW-UAV speeds under the generalized logistic model are smaller than the corresponding ones under the logistic model. From a formal point of view, this is the reason for the reduced energy consumption experienced under the generalized logistic model.

7.2. Performance comparisons against baselines – an ablation study

The main goal of the ablation study carried out in this section is to address the following question: what is the trajectory parameter whose optimization has the largest impact on the resulting RW-UAV energy performance? To address this question, the following three partially optimized BaSelines (BSs) have been implemented and simulated:

BS#1 Under this baseline, the trajectory radius R is *not* optimized but it is randomly selected over its feasible range. For each generated R outcome, the corresponding H and T_P parameters are *jointly* optimized through a suitably modified version of the primal-dual iterations of Eqs. (44) and (45) and the resulting propulsion en-

Table 4
Optimized values for the RW-UAV trajectory parameters and propulsion energy at path-loss thresholds of: *(a)* 155 (dB); *(b)* 150 (dB); and, *(c)* 145 (dB). Case of logistic *LoS* probability model at $P_{OUT} = 0.2$.

(a)

Environment	R (m)	H (m)	v (m/s)	$\mathscr{E}_P$ (J)
Sub-Urban	1.04	350.00	2.94	2137.0
Urban	2.36	350.00	5.44	2436.6
Dense Urban	5.99	350.00	10.52	3077.1
High rise Urban	7.22	350.00	11.99	3254.7

(b)

Environment	R (m)	H (m)	v (m/s)	$\mathscr{E}_P$ (J)
Sub-Urban	3.60	89.71	7.24	2694.6
Urban	7.89	140.67	12.75	3348.2
Dense Urban	9.96	350.00	14.91	3617.4
High rise Urban	10.02	350.00	14.94	3624.7

(c)

Environment	R (m)	H (m)	v (m/s)	$\mathscr{E}_P$ (J)
Sub-Urban	7.96	54.83	12.71	3358.0
Urban	8.02	132.02	12.90	3365.3
Dense Urban	10.07	350.00	15.03	3631.8
High rise Urban	10.32	350.00	15.24	3661.8

Table 5
Optimized values of the RW-UAV trajectory parameters and propulsion energy under the generalized logistic *LoS* probability model at $TH_{PL} = 155$ (dB). Case of Urban environment.

P_{OUT}	R (m)	H (m)	v (m/s)	$\mathscr{E}_P$ (J)
1.0×10^{-4}	1.04	62.17	2.89	2157.1
1.0×10^{-3}	1.04	318.87	2.95	2130.0
1.0×10^{-2}	1.04	350.00	3.13	2056.6
1.0×10^{-1}	1.04	350.00	3.22	2029.3
2.0×10^{-1}	1.04	350.00	3.37	1990.6

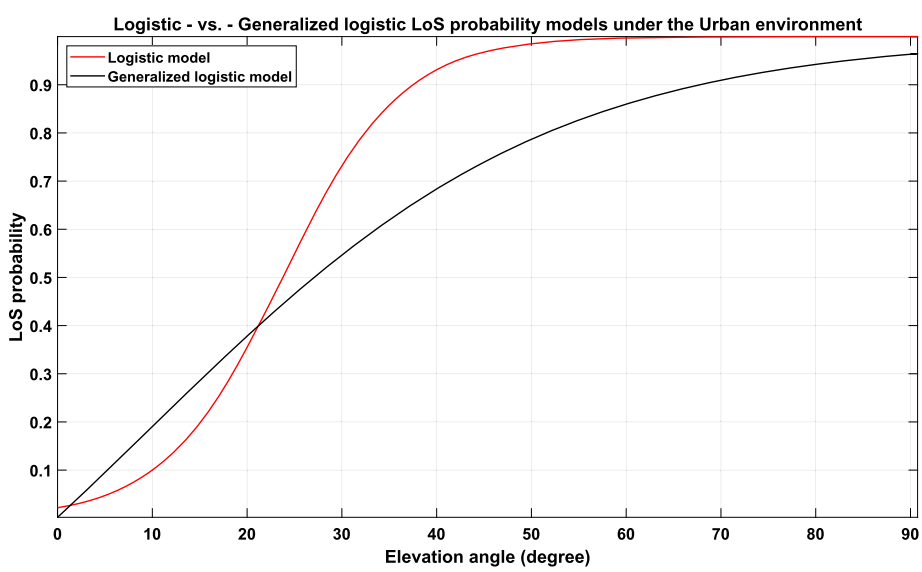

Fig. 8. Numerically evaluated behaviors of the logistic and generalized logistic *LoS* probability models. Case of Urban environment.

ergy is numerically computed. Then, the average energy: $\bar{\mathscr{E}}_P^{BS\#1}$ obtained over 10^6 independent trials is numerically evaluated;

BS#2 Under this baseline, the altitude parameter H is not optimized but it is randomly selected over its feasible range. For each generated outcome of H, the corresponding R and T_P parameters are jointly optimized. The obtained average energy is indicated by $\bar{\mathscr{E}}_P^{BS\#2}$; and

BS#3 Under this baseline, the trajectory period T_P is not optimized but it is randomly selected over its feasible range. For each generated T_P outcome, the corresponding R and H parameters are jointly optimized. The obtained average energy is indicated by $\bar{\mathscr{E}}_P^{BS\#3}$.

Table 6 reports the obtained average energies of these baselines under the logistic *LoS* probability model at $TH_{PL} = 155$ (dB) and $P_{OUT} = 0.2$.

Table 6
Average energy performance of the considered baselines under the logistic LoS probability model at $P_{OUT} = 0.2$ and $TH_{PL} = 155$ (dB).

Environment	$\overline{\mathscr{E}}_P^{BS\#1}$ (J)	$\overline{\mathscr{E}}_P^{BS\#2}$ (J)	$\overline{\mathscr{E}}_P^{BS\#3}$ (J)
Sub-Urban	2478.9	2243.8	2350.7
Urban	2875.2	2582.8	2704.6
Dense Urban	3692.5	3323.3	3477.1
High rise Urban	3970.7	3580.2	3742.9

Table 7
BFS-BS performance at $TH_{PL} = 155$ (dB).

Environment	$R^{(BFS)}$ (m)	$H^{(BFS)}$ (m)	$v^{(BFS)}$ (m/s)	$\mathscr{E}_{MIN}^{(BFS)}$ (J)
Sub-Urban	1.17	67.96	3.52	2072.9
Urban	1.79	310.59	4.25	2363.7
Dense Urban	3.72	216.60	6.05	2984.8
High rise Urban	6.52	310.35	11.13	3157.1

Table 8
Experienced execution times. $\square^{(*)}$: = Measured execution time; $\square^{(**)}$: = Forecast execution time.

Optimizer	HW Execution Platform	Execution Time (in (s))
Proposed iterative optimizer	*Single-core sequential execution platform*	$0.44^{(*)}$
BFS-BS	*64-core parallel execution platform*	$5593^{(*)}$
BFS-BS	*Single-core sequential execution platform*	$\approx 318800^{(**)}$

A comparison of the entries of Table 6 with the corresponding ones of Table 4a unveils that the average energy values: $\overline{\mathscr{E}}_P^{BS\#1}$ returned by $BS\#1$ are larger than the corresponding ones of Table 4a of about 16%, 18%, 20%, and 22% under the Sub-Urban, Urban, Dense Urban, and High rise Urban environments respectively. The corresponding energy gaps suffered from $BS\#2$ (resp., $BS\#3$) are around 5%, 6%, 8%, and 10% (resp., 10%, 11%, 13%, and 15%).

These results allow us to draw the following three main conclusions about the relative impact of the separated-vs.-joint optimization of the trajectory parameters. First, the RW-UAV energy performance is mostly (resp., less) sensitive on the optimization of the trajectory radius (resp., trajectory altitude). Second, the energy savings that are obtained via the joint optimization of all three trajectory parameters are more (resp., less) noticeable under the more (resp., less) challenging High rise Urban (resp., Sub-Urban) environment. Finally, the energy savings that are attained through the joint optimization of all three trajectory parameters compared to the corresponding ablated cases maintain over 5% and reach 22%.

7.3. Performance comparison against a brute-force search benchmark

As pointed out in Section 3.3, the goal of this section is to numerically evaluate the energy increment induced by the replacement of the single (weaker) constraint in Eq. (19) with the coupled (stronger) ones in Eqs. (20) and (21). To address this question, we have implemented and tested the performance of the following Brute Force Search-based BaSeline (*BFS-BS*):

$BFS\text{-}BS$: the range of the allowed values of each trajectory parameter R, H, and T_P is endowed with a one-dimensional grid of 300 evenly-spaced references points to generate a 3D lattice of: $300^3 \equiv 2.7 \times 10^7$ candidate parameter 3-plets $\{R, H, T_P\}$. Afterwards, the feasibility of each 3-*plet* is checked by *directly* testing the original non-convex path-loss constraint in Eq. (19) together with the ones in Eqs. (16), (17), (18), (23), and (24). If the generated 3-*plet* is feasible, the corresponding energy consumption is directly evaluated through the original non-convex model in Eqs. (14) and (15). Finally, the *lowest* (minimum) energy value: $\mathscr{E}_{MIN}^{(BFS)}$ obtained through the brute-force search over the built-up 3D lattice is returned.

These computed $\mathscr{E}_{MIN}^{(BFS)}$'s values are reported in Table 7 under the logistic LoS probability model at $TH_{PL} = 155$ (dB).

A comparison of the entries of Table 7 with the corresponding ones of Tables 4a, 4b, and 4c allows us to conclude that the energy consumption under the implemented *BFS-BS* are somewhat lower than the ones obtained by the proposed optimizer at $P_{OUT} = 0.2$, but the gaps remain limited up to 3% - 4%. Interestingly, in all tests, the $BFS - BS$ never returned the RW-UAV hovering state as the most energy-saving one, thus supporting the actual effectiveness of the performed trajectory optimization. However, the experienced reduction in the energy consumption provided by the implemented $BFS - BS$ is counter-balanced by two main drawbacks. First, the (numerically evaluated) values of the out-of-service probability: $P_{OUT}^{(BFS)}$ returned by the BFS-BS are somewhat larger than 0.2 and typically fall in the interval: 0.25 - 0.30. This confirms that the adoption of the (weaker) constraint in Eq. (19) does *not* longer allow to enforce thresholds on the desired target out-of-service probability. Second, the experienced execution times reported in Table 8 support the conclusion that the proposed iteration-based optimizer of Section 5 is implementable on small size UAVs that are equipped with low-end single-core (Raspberry Pi-based) CPUs [5] (see the first row of Table 8). On the contrary, the corresponding implementation of the competing *BFS* baseline would be very challenging (or even infeasible at all; see the last two rows of Table 8).

7.4. Rotary Wing-vs.-Fixed Wing UAV optimized performance

Let us consider now the companion case in which the serving UAV in Fig. 1 is of Fixed-Wing (FW) type [5]. Then, according to [22], the resulting per-period propulsion energy: $\mathscr{E}_P^{(FW)}$ (J) reads as in:

$$\mathscr{E}_P^{(FW)} \triangleq T_P \times \mathscr{P}_P^{(FW)} \equiv T_P \times \left(\beta_1 v^3 + \frac{\beta_2}{v}\left(1 + \frac{{a_c}^2}{g^2}\right)\right), \tag{54}$$

where: β_1 (measured in $\left((\frac{\mathrm{s}}{\mathrm{m}})^3 \times \mathrm{W}\right)$), and: β_2 (measured in $\left((\frac{\mathrm{m}}{\mathrm{s}}) \times \mathrm{W}\right)$) are positive constants that depend on the propulsion power profile of the considered FW-UAV (see, for example, the final appendix of [22] for more details on this topic). Hence, since the speed v and the centrifugal acceleration a_c in Eq. (54) are still given by Eq. (14), the resulting optimization problem:

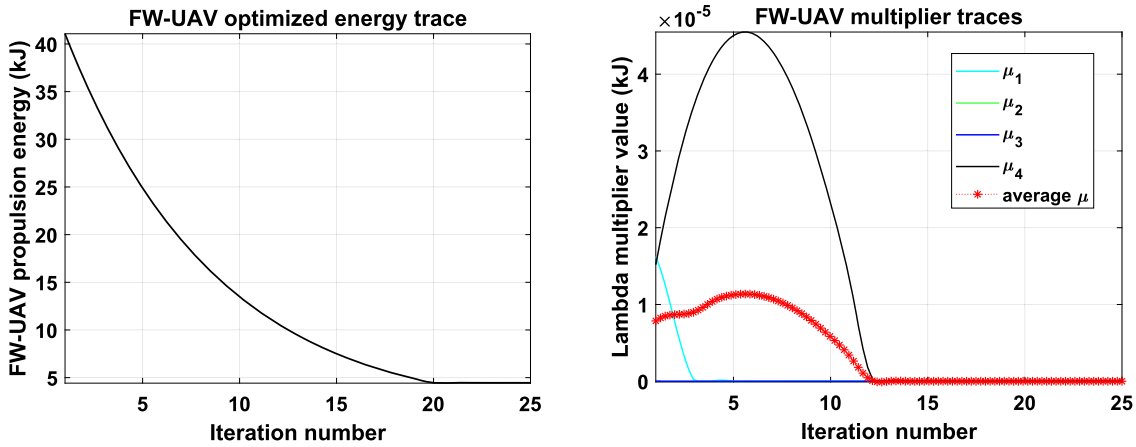

(a) (b)

Fig. 9. Dynamic behaviors of the simulated FW-UAV energy curve and the corresponding Lagrange multipliers associated to the constraints in Eqs. (17), (18), (23), and (24). Case of the logistic LoS probability model under the High rise Urban environment at $TH_{PL} = 145\,(\text{dB})$ and $P_{OUT} = 0.2$.

Table 9
Optimized performance of the simulated FW-UAV under the logistic LoS probability model. *(a)* Case of $P_{OUT} = 0.2$ and $TH_{PL} = 145\,(\text{dB})$; (b) Case of $P_{OUT} = 0.2$ and $TH_{PL} = 155\,(\text{dB})$; (c) Case of $P_{OUT} = 0.01$ and $TH_{PL} = 145\,(\text{dB})$; (d) Case of $P_{OUT} = 0.01$ and $TH_{PL} = 155\,(\text{dB})$.

(a)

Environment	$R^{(FW)}$ (m)	$H^{(FW)}$ (m)	$v^{(FW)}$ (m/s)	$\mathscr{E}_P^{(FW)}$ (J)
Sub-Urban	18.44	350.00	16.27	3197.4
High rise Urban	20.38	350.00	19.87	3761.2

(b)

Environment	$R^{(FW)}$ (m)	$H^{(FW)}$ (m)	$v^{(FW)}$ (m/s)	$\mathscr{E}_P^{(FW)}$ (J)
Sub-Urban	1.04	350.00	13.16	2882.7
High rise Urban	19.98	350.00	19.09	3622.8

(c)

Environment	$R^{(FW)}$ (m)	$H^{(FW)}$ (m)	$v^{(FW)}$ (m/s)	$\mathscr{E}_P^{(FW)}$ (J)
Sub-Urban	19.38	350.00	20.87	3861.4
High rise Urban	21.21	350.00	21.53	4080.3

(d)

Environment	$R^{(FW)}$ (m)	$H^{(FW)}$ (m)	$v^{(FW)}$ (m/s)	$\mathscr{E}_P^{(FW)}$ (J)
Sub-Urban	21.38	350.00	18.87	3661.2
High rise Urban	20.79	350.00	20.68	3913.5

$$\textbf{P3:} \quad \min_{\{R,\,H,\,T_P\}} \quad \mathscr{E}_P^{(FW)}, \tag{55a}$$

$$\text{s.t.:} \quad \text{Eqs. (16), (17), (18), (23) and (24),} \tag{55b}$$

is *already* in GP form, then its solution may be numerically evaluated by a *direct* application of the primal-dual optimization approach [47]. Therefore, by using the Lagrangian function of the problem in P3, we have implemented the resulting primal-dual iterations by still resorting to the proposed relationship in Eq. (47) for the adaptive computation of the involved step-sizes. By doing so, we have obtained the dynamic traces of Fig. 9, together with the optimized trajectory parameters of Table 9. For the purpose of comparison, in all conducted tests, the power-profile constants β_1 and β_2 in Eq. (54) have been set as in Table I of [54] (see also Table A.10 in the Appendix A).

The plots of Fig. 9 confirm that, under the proposed adaptive step-size design, a number of primal-dual iterations limited up to 20–25 suffices for the stable convergence of the energy and multiplier traces even under the energy profile of Eq. (54). Furthermore, a comparison of the entries of Table 9 with the corresponding ones of Tables 3a and 3d allows us to draw the following final conclusions about the RW-UAV-vs.-FW-UAV optimized trajectory parameters and related energy performance:

(i) the FW-UAV performance is not so sensitive to the optimization of the trajectory altitude, which in all cases of Table 9 remains, indeed, fixed at $H^{(FW)} = 350\,(m)$;
(ii) the optimized speeds of the simulated FW-UAV are larger than the corresponding ones of the tested RW-UAV of about 2 - 3 times, specially under the (less challenging) Sub-Urban environment;
(iii) the (optimized) propulsion energy wasted by the simulated FW-UAV is larger than the corresponding ones of the considered RW-UAV of about 12% under the (most challenging) High rise Urban environment at both $P_{OUT} = 0.2$ and $P_{OUT} = 0.01$; and
(iv) the corresponding FW-UAV energy is larger than the RW-UAV ones up to 34.9% (resp., 26.6%) at $P_{OUT} = 0.2$ (resp., $P_{OUT} = 0.01$) under the (less challenging) Sub-Urban environment.

The above (simulated) results seem to be well aligned with real-world measurements [2,4,54].

8. Conclusions and hints for future research

The focus of this paper is on the energy-saving optimization of the 3D trajectory parameters of a RW-UAV, which flies along a circular trajectory for providing wireless coverage to a number of randomly deployed GUs. In a nutshell, the main contributions are: (i) the development of a formal procedure for the convexification of the *acceleration-dependent* energy profile of the RW-UAV under a number of system constraints, which embrace wireless coverage, maximum tolerated path-loss, QoS-dictated target in-service-probability, and UAV antenna beam-width; and (ii) the joint design of suitable SDN/NFV-based virtualized architectures at the flying UAV and GCS for the support of the demanded services. Extensive performance comparisons with a number of baselines confirmed the actual effectiveness of the developed optimization framework.

Being the inclusion of acceleration-dependent propulsion energy models in the performance analysis of RW UAV-supported networked computing systems still in its infancy, we believe that the presented results could be extended along (at least) four main research directions.

First, the afforded optimization problem could be extended to the case, where the RW-UAV follows an *arbitrary* (non-circular) acceleration-dependent 3D trajectory. In this regard, the main expected challenge is the generalization (if feasible) of the developed approach for the convexification of the resulting RW-UAV propulsion energy under arbitrary trajectories.

Second, the present contribution affords the basic case of a *single* serving RW-UAV. How to manage the additional constraints, arising from the simultaneous (and cooperative) energy-aware optimization of the acceleration-dependent trajectories of multiple serving RW-UAVs could be an additional research hint.

Third, a future research line may embrace the overall energy-aware design of virtualized UAV-supported ecosystems in the realm of the so-called Internet of Drones (IoD) [4,5,55]. In this regard, using virtualized UAV-mounted Fog computing servers in the radio access network for providing mobile computing/communication support to resource-limited IoT devices is a promising but still quite new approach, for which it is still not clear to what extent edge computing can push the state-of-the-art communication-computing technology to utilize its full potential in an energy-aware way.

Finally, by referring to the virtualized UAV architecture proposed in Figs. 4 and 5, a last research topic may regard the development of suitable algorithms and related implementation protocols for the inter-container live (e.g., real-time) migration of the services required by the GUs when new service arrivals happen, and, then, re-scheduling and/or re-embedding of the under-execution services is demanded, in order to re-optimize the UAV resource usage [18].

Declaration of competing interest

The authors declare that they have no known competing financial interests or personal relationships that could have appeared to influence the work reported in this paper.

Data availability

Data will be made available on request.

Acknowledgement

This work has been supported by the projects: "DeepFog – Optimized distributed implementation of Deep Learning models over networked multi-tier Fog platforms for IoT stream applications" and "Flying Fog (FF): when the Fog learns to fly" funded by Sapienza University of Rome - Bando 2020, 2021, and 2022, under grants RM12017294171495, RM12117A39E2E9A7, and RM122180FB3CA3F2, respectively. The work is also partially supported by the research collaboration with the Institute of Informatics and Telematics (IIT-CNR) on the theme: "Design and software development of Fog Computing platforms for the support of Deep Learning algorithms for the real-time image analysis".

Appendix A. Paper taxonomy and default setting of the main simulated parameters

Table A.10 provides a synoptic recap of the main paper's taxonomy together with the setting of the main simulated parameters.

Appendix B. Proofs of the problem feasibility conditions

In this Appendix, we detail the proofs of the feasibility conditions reported in the Propositions 1, 2 and 3 of Section 4.

Necessary part of Proposition 1. The proof is by contradiction.Hence, let us assume that the l.h.s. of Eq. (28) is strictly negative. Then, since the tangent-dependent term is positive by design, the constraint in Eq. (17) on R would be infeasible for all values of H falling in the interval: $\left[H^{(MIN)},\ H^{(MAX)}\right]$ and all values of R falling in the allowed interval (see Eq. (27)): $\left[0,\ \min\left\{R_C\ ;\ \left(v^{(MAX)}T_P^{(MAX)}/2\pi\right)\right\}\right]$. Thus, since we arrived to a contradiction, the necessary part of the condition in Eq. (28) is proved. □

Sufficient part of Proposition 1. Let the condition in Eq. (28) be met and let us consider the following values for the trajectory radius and altitude:

$$R \equiv R^{(MAX)} \quad \text{and} \quad H \equiv H^{(MAX)}, \tag{B.1}$$

with $R^{(MAX)}$ defined as in Eq. (32). Since, by inspection, the setting in Eq. (B.1) meets all the constraints in Eqs. (16) and (17) and also the previously considered constraints in Eq. (27), we conclude that this setting is feasible under all these constraints. This proves the sufficient part of Proposition 1. In this regard, we note that $R^{(MAX)}$ in Eq. (32) plays the role of the maximum value allowed the trajectory radius under the *overall* set of constraints of Eq. (26b). □

Necessary part of Proposition 2. The box constraints in Eqs. (36d) - (36f) guarantee that the following chain of inequalities holds:

$$\left(H\Big/(R+R_C)\right) \le \left(H^{(MAX)}\Big/\left(R+R_C\right)\right) \le \left(H^{(MAX)}\Big/R_C\right), \tag{B.2}$$

that, in turn, directly proves the necessary part of Proposition 2. □

Sufficient part of Proposition 2. The trajectory radius is upperbounded by $R^{(MAX)}$ in Eq. (32) and this guarantees that:

$$(H\Big/(R+R_C)) \ge (H^{(MIN)}\Big/\left(R^{(MAX)}+R_C\right)). \tag{B.3}$$

Hence, after introducing the term at the r.h.s. of the above inequality into the l.h.s. of Eq. (23), we directly arrive at Eq. (31). □

Proposition 3. Under already considered constraints, the following upper and lower bounds hold for the expression at the l.h.s. of Eq. (24):

$$\begin{aligned} B_0\left[H^{(MIN)^2}+R_C{}^2\right]-1 &\le B_0\left[H^2+\ (R+R_C)^2\right]-1 \\ &\le B_0\left[H^{(MAX)^2}+\ \left(R^{(MAX)}+R_C\right)^2\right]-1. \end{aligned} \tag{B.4}$$

Therefore, after replacing the l.h.s. of Eq. (24) with the lower (resp., upper) bound in Eq. (B.4), we directly arrive at the necessary (resp., sufficient) feasibility condition in Eq. (33) (resp., in Eq. (34)). □

Table A.10
Main paper's taxonomy, unit of measurement and default setting of the main simulated parameters.

Main System Parameters		
Symbol	Meaning/Role	Simulated setting
$v^{(MAX)}$	UAV maximum allowed linear speed	70.0 (m/s)
$T_P^{(MAX)}$	UAV maximum allowed trajectory period	13.0 (s)
$H^{(MAX)}$, $H^{(MIN)}$	UAV maximum and minimum allowed altitudes	350 (m), 30 (m)
Φ_{UAV}	UAV antenna half-power beamwidth	80 (deg)
R_C	Required coverage radius	400 (m)
$P_{OUT} \equiv 1 - P_{SER}$	Maximum tolerated outage probability	{0.2, 0.1, 0.01, 0.001, 0.0001}
B, η_{LoS} (dB), C (deg), η_{NLoS} (dB)	Parameters of the logistic LoS probability model	As in Table 2
$B1$, $B2$, $B3$, $B4$	Parameters of the generalized logistic LoS probability model	−0.4568, 0.0470, −0.63, 1.63
g, f_c, δ, c	Gravitational acceleration, carrier frequency, path-loss exponent, and light speed	9.81 $(\mathrm{m/s^2})$, 2.5 (GHz), 2.5, 3.0×10^8 (m/s)
γ_1, γ_2, γ_3, γ_4, γ_5	Propulsion power-profile parameters of the simulated RW-UAV	504.6 (W), $6.53 \times 10^{-5} (\mathrm{m/s})^2$, 6.53×10^{-3} $((\mathrm{m/s})^3 \times (\mathrm{W}))$, 687.88 (W), $90.20 (\mathrm{m/s})^2$
a_0, a_1, $I^{(MAX)}$	Step-size regularizing parameters and maximum primal-dual iteration number	0.2, 1.5, 30
β_1, β_2	Propulsion power-profile parameters of the simulated FW-UAV	9.26×10^{-4} $((\mathrm{m/s})^{-3} \times (\mathrm{W}))$, 2250 $((\mathrm{m/s}) \times (\mathrm{W}))$
Optimized Variables		
Symbol	Meaning/Role	
R, H, T_P	Optimized UAV trajectory radius (in (m)), altitude (in (m)), and period (in (s)). They are the primal optimization variables.	
ω and v	Optimized UAV angular speed (in (rad/s)) and linear speed (in (m/s)).	
$d^{(MAX)}$ and $\theta^{(MIN)}$	Optimized UAV-GU maximum distance (in (m)) and minimum elevation angle (in (deg)).	
$\mathscr{E}_P$ and $\mathscr{P}_P$	Optimized UAV propulsion energy (in (J)) and power (in (W)).	

Appendix C. Turning the *P1* optimization problem into GP form

Let us consider the acceleration-dependent power model of Eq. (11) with a_c and v as in Eq. (14). In order to convexify this model, let us introduce two non-negative scalar-valued slack variables y and z, which are defied as in:

$$\frac{1}{y^2} \triangleq 1 + \frac{a_c^2}{g^2}, \tag{C.1}$$

and

$$z^2 \triangleq \left(1 + \frac{a_c^2}{g^2} + \frac{v^4}{\gamma_5^2}\right)^{\frac{1}{2}} - \frac{v^2}{\gamma_5} \overset{(a)}{\equiv} \left(\frac{1}{y^2} + \frac{v^4}{\gamma_5^2}\right)^{\frac{1}{2}} - \frac{v^2}{\gamma_5}, \tag{C.2}$$

where (a) in Eq. (C.2) follows from the definition in Eq. (C.1). Hence, after expressing the propulsion energy in Eq. (15) in the following equivalent (but more compact) form:

$$\mathscr{E}_P = \gamma_1 T_P \left(1 + \gamma_2 v^2\right) + \gamma_3 T_P v^3 + \frac{\gamma_4 T_P z}{y}, \tag{C.3}$$

we note that (see the definition in Eq. (C.2)):

$$\left(z^2 + \frac{v^2}{\gamma_5}\right)^2 = \frac{1}{y^2} + \frac{v^4}{{\gamma_5}^2}, \tag{C.4}$$

that, in turn, may be equivalently rewritten as the following equality constraint:

$$\frac{1}{y^2 z^4} = 1 + 2\,\frac{v^2}{z^2 \gamma_5}. \tag{C.5}$$

Now, we prove that, since our ultimate task is the minimization of $\mathscr{E}_P$ in Eq. (C.3), *without loss of optimality*, we may replace the equality constraint in Eq. (C.5) with the following inequality one:

$$\frac{1}{y^2 z^4} \leq 1 + 2\,\frac{v^2}{z^2 \gamma_5}. \tag{C.6}$$

Since the proof is by contradiction, let us assume that, at the optimum, the constraint in Eq. (C.6) is met with the strict inequality. Then, we may decrease the corresponding value of z, in order to both: (i) guarantee that the constraint in (C.6) is met with the equality; and, (ii) reduce the corresponding value of $\mathscr{E}_P$ in Eq. (C.3). So doing, we arrive to a contradiction.

Finally, since Eq. (C.6) can be reworked as in (see the definition of the constant c_0 in Eqs. (38a) and (38b)): $\left(1/y^2\, z^4\right) \leq c_0$, we arrive to the following first inequality constraint on the slack variables:

$$\frac{y^{-2} z^{-4}}{c_0} \leq 1. \tag{C.7}$$

Since c_0 is non-negative (see Eq. (38a)), this constraint is in monomial form.

Let us consider the relationship in Eq. (C.1). Although it enforces a nonlinear equality constraint on the slack variable y, we now prove that, *without loss of optimality*, it may be rewritten in the following equivalent form:

$$\frac{1}{y^2} \geq 1 + \frac{a_c^2}{g^2}. \tag{C.8}$$

Being also the proof of the equivalence of the constraints in Eqs. (C.1) and (C.8) by contradiction, let us assume that, at the optimum (when $\mathscr{E}_P$ in (C.3) attains its minimum), the relationship in Eq. (C.8) is met with the strict inequality. Hence, we may increase y for meeting Eq. (C.8) with the equality. However, by doing so, we decrease $\mathscr{E}_P$ in (C.3) and this contradicts the assumed optimality of $\mathscr{E}_P$.

Lastly, we observe that: (i) the expression in (C.3) of the propulsion energy is posynomial in the involved variables: T_P, $v \equiv \left(2\pi/T_P\right) R$, z, and y; (ii) since a_c in Eq. (C.8) is monomial in the variables R and T_P (see the definition in Eq. (14)), both the constraints in Eqs. (C.7) and (C.8) are posynomial in the involved variables; and (iii) all the previously considered system constraints in Eqs. (16), (17), (18), (23) and (24) are already monomial or posynomial functions. Therefore, after in-

troducing the log-transformed variables of Eq. (35), we arrive at the GP formulation in Eq. (36) of the optimization problem in *P2*.

Appendix D. Limit properties of the proposed step-size of Eq. (47)

The proposed step-size in Eq. (47) retains the following set of limit properties:

$$\lim_{|\partial_u \mathscr{L}|\to 0} g_u \equiv \lim_{|\partial_u \mathscr{L}|\to 0} \frac{a_0}{\sqrt{a_1}}\left[1-\frac{(\partial_u \mathscr{L})^2}{2a_1}\right] \equiv \frac{a_0}{\sqrt{a_1}} \triangleq g^{(MAX)}, \tag{D.1}$$

$$\lim_{|\partial_u \mathscr{L}|\to 0} g_u \times \partial_u \mathscr{L} \equiv \lim_{|\partial_u \mathscr{L}|\to 0} \frac{a_0}{\sqrt{a_1}} \times \partial_u \mathscr{L}, \tag{D.2}$$

$$\lim_{|\partial_u \mathscr{L}|\to \infty} g_u \equiv \lim_{|\partial_u \mathscr{L}|\to \infty} \frac{a_0}{|\partial_u \mathscr{L}|} \equiv 0 \triangleq g^{(MIN)}, \tag{D.3}$$

$$\lim_{|\partial_u \mathscr{L}|\to \infty} g_u \times \partial_u \mathscr{L} \equiv \lim_{|\partial_u \mathscr{L}|\to \infty} a_0 \times \frac{\partial_u \mathscr{L}}{|\partial_u \mathscr{L}|} \equiv a_0 \times \mathrm{sign}(\partial_u \mathscr{L}). \tag{D.4}$$

These formal properties guarantee that:

(i) the maximum value: $g^{(MAX)}$ of g_u is non-vanishing and, as it could be desirable, it is attained for vanishing values of $\partial_u \mathscr{L}$ (see Eq. (D.1)). This could allow the primal-dual iterations of Eqs. (44) and (45) to *speed up* the convergence rate when they are approaching their global minimum, as well as to *quickly react* to possible abrupt changes of the parameter setting after reaching the steady-state;

(ii) g_u scales up gently for vanishing $\partial_u \mathscr{L}$ as (see Eq. (D.1)): $\mathscr{O}\left(1-(\partial_u \mathscr{L})^2\right)$. This property allows the primal-dual iterations to attain *stable* convergence;

(iii) according to Eq. (D.2), the resulting product: $(g_u \times \partial_u \mathscr{L})$ scales down proportionally to $\partial_u \mathscr{L}$. This property would facilitate a *fine-tuning* search of the actual global minimum when the primal-dual iterations are approaching it; and,

(iv) when $|\partial_u \mathscr{L}|$ grows unbounded, g_u vanishes to avoid unstable behaviors (see Eq. (D.3)). However, above all, Eq. (D.4) guarantees that the resulting product: $(g_u \times \partial_u \mathscr{L})$ maintains *limited* up to: a_0, while it continues to retain the sign of $\partial_u \mathscr{L}$.

References

[1] X. You, C. Wang, et al., Towards 6G wireless communication networks: vision, enabling technologies, and new paradigm shifts, Sci. China Inf. Sci. 64 (2021) 110301, https://doi.org/10.1007/s11432-020-2955-6.

[2] H. Jin, X. Jin, et al., A survey of energy efficient methods for UAV communication, Veh. Commun. 41 (2023) 100594, https://doi.org/10.1016/j.vehcom.2023.100594.

[3] Y. Zeng, Q. Wu, R. Zhang, Accessing from the sky: a tutorial on UAV communications for 5G and beyond, Proc. IEEE 107 (12) (2019) 2327–2375, https://doi.org/10.1109/JPROC.2019.2952892.

[4] N. Nomikos, E.T. Michailidis, et al., A UAV-based moving 5G RAN for massive connectivity of mobile users and IoT devices, Veh. Commun. 25 (2020) 100250, https://doi.org/10.1016/j.vehcom.2020.100250.

[5] R.A. da Silva, N.L. da Fonseca, Location of fog nodes mounted on fixed-wing UAVs, Veh. Commun. 41 (2023) 100600, https://doi.org/10.1016/j.vehcom.2023.100600.

[6] Aerial base stations with opportunistic links for unexpected and temporary events (ABSOLUTE), https://www.airbornecomms.com/absolute-project. (Accessed April 2023).

[7] Y. Zeng, I. Guvenc, et al. (Eds.), UAV Communications for 5G and Beyond, 1st edition, Wiley-IEEE Press, 2021.

[8] X. Jiang, M. Sheng, et al., Green UAV communications for 6G: a survey, Chin. J. Aeronaut. 35 (9) (2022) 19–34, https://doi.org/10.1016/j.cja.2021.04.025.

[9] W. Fawaz, Effect of non-cooperative vehicles on path connectivity in vehicular networks: a theoretical analysis and UAV-based remedy, Veh. Commun. 11 (2018) 12–19, https://doi.org/10.1016/j.vehcom.2018.01.005.

[10] W. Saad, M. Bennis, et al., Wireless Communications and Networking for Unmanned Aerial Vehicles, 1st edition, Cambridge University Press, 2020.

[11] Y. Zeng, J. Xu, et al., Energy minimization for wireless communication with rotary-wing UAV, IEEE Trans. Wirel. Commun. 18 (4) (2019) 2329–2345, https://doi.org/10.1109/TWC.2019.2902559.

[12] C. Zhan, H. Lai, Energy minimization in Internet-of-things system based on rotary-wing UAV, IEEE Wirel. Commun. Lett. 8 (5) (2019) 1341–1344, https://doi.org/10.1109/LWC.2019.2916549.

[13] N. Gao, Y. Zeng, et al., Energy model for UAV communications: experimental validation and model generalization, China Commun. 18 (7) (2021) 253–264, https://doi.org/10.23919/JCC.2021.07.020.

[14] X. Dai, B. Duo, et al., Energy-efficient UAV communications: a generalized propulsion energy consumption model, IEEE Wirel. Commun. Lett. 11 (10) (2022) 2150–2154, https://doi.org/10.1109/LWC.2022.3195787.

[15] P.K. Singh, S.K. Nandi, S. Nandi, A tutorial survey on vehicular communication state of the art, and future research directions, Veh. Commun. 18 (2019) 100164, https://doi.org/10.1016/j.vehcom.2019.100164.

[16] H. Zhou, H. Wang, et al., Data offloading techniques through vehicular ad hoc networks: a survey, IEEE Access 6 (2018) 65250–65259, https://doi.org/10.1109/ACCESS.2018.2878552.

[17] F. Al-Turjman, M. Abujubbeh, et al., UAVs assessment in software-defined IoT networks: an overview, Comput. Commun. 150 (2020) 519–536, https://doi.org/10.1016/j.comcom.2019.12.004.

[18] O.S. Oubbati, M. Atiquzzaman, et al., Softwarization of UAV networks: a survey of applications and future trends, IEEE Access 8 (2020) 98073–98125, https://doi.org/10.1109/ACCESS.2020.2994494.

[19] A. Al-Hourani, S. Kandeepan, A. Jamalipour, Modeling air-to-ground path loss for low altitude platforms in urban environments, in: Proceedings of 2014 IEEE Global Communications Conference, GLOCOM'14, IEEE, Austin, TX, USA, 2014, pp. 2898–2904.

[20] M. Mozaffari, W. Saad, et al., Drone small cells in the clouds: design, deployment and performance analysis, in: Proceedings of 2015 IEEE Global Communications Conference (GLOBECOM), IEEE, San Diego, CA, USA, 2015, pp. 6–10.

[21] C. You, R. Zhang, Hybrid offline-online design for UAV-enabled data harvesting in probabilistic LoS channels, IEEE Trans. Wirel. Commun. 19 (6) (2020) 3753–3768, https://doi.org/10.1109/TWC.2020.2978073.

[22] Y. Zeng, R. Zhang, Energy-efficient UAV communication with trajectory optimization, IEEE Trans. Wirel. Commun. 16 (6) (2017) 3747–3760, https://doi.org/10.1109/TWC.2017.2688328.

[23] Z.M. Fadlullah, D. Takaishi, et al., A dynamic trajectory control algorithm for improving the communication throughput and delay in UAV-aided networks, IEEE Netw. 30 (1) (2016) 100–105, https://doi.org/10.1109/MNET.2016.7389838.

[24] F. Ono, H. Ochiai, R. Miura, A wireless relay network based on unmanned aircraft system with rate optimization, IEEE Trans. Wirel. Commun. 15 (11) (2016) 7699–7708, https://doi.org/10.1109/TWC.2016.2606388.

[25] D. Yang, Q. Wu, et al., Energy tradeoff in ground-to-UAV communication via trajectory design, IEEE Trans. Veh. Technol. 67 (7) (2018) 6721–6726, https://doi.org/10.1109/TVT.2018.2816244.

[26] M. Alzenad, A. El-Keyi, H. Yanikomeroglu, 3-D placement of an unmanned aerial vehicle base station for maximum coverage of users with different QoS requirements, IEEE Wirel. Commun. Lett. 7 (1) (2018) 38–41, https://doi.org/10.1109/LWC.2017.2752161.

[27] C.-C. Lai, C.-T. Chen, L.-C. Wang, On-demand density-aware UAV base station 3D placement for arbitrarily distributed users with guaranteed data rates, IEEE Wirel. Commun. Lett. 8 (3) (2019) 913–916, https://doi.org/10.1109/LWC.2019.2899599.

[28] M. Liu, J. Yang, G. Gui, Dsf-noma: Uav-assisted emergency communication technology in a heterogeneous Internet of things, IEEE Int. Things J. 6 (3) (2019) 5508–5519, https://doi.org/10.1109/JIOT.2019.2903165.

[29] L. Zhang, N. Ansari, Approximate algorithms for 3-D placement of IBFD enabled drone-mounted base stations, IEEE Trans. Veh. Technol. 68 (8) (2019) 7715–7722, https://doi.org/10.1109/TVT.2019.2923143.

[30] Q. Wu, Y. Zeng, R. Zhang, Joint trajectory and communication design for multi-UAV enabled wireless networks, IEEE Trans. Wirel. Commun. 17 (3) (2018) 2109–2121, https://doi.org/10.1109/TWC.2017.2789293.

[31] W. Shi, J. Li, et al., Multi-drone 3-D trajectory planning and scheduling in drone-assisted radio access networks, IEEE Trans. Veh. Technol. 68 (8) (2019) 8145–8158, https://doi.org/10.1109/TVT.2019.2925629.

[32] E. Baccarelli, M. Scarpiniti, A. Momenzadeh, EcoMobiFog–design and dynamic optimization of a 5G mobile-fog-cloud multi-tier ecosystem for the real-time distributed execution of stream applications, IEEE Access 7 (2019) 55565–55608, https://doi.org/10.1109/ACCESS.2019.2913564.

[33] N. Madan, A.W. Malik, et al., On-demand resource provisioning for vehicular networks using flying fog, Veh. Commun. 25 (2020) 100252, https://doi.org/10.1016/j.vehcom.2020.100252.

[34] R.A.C. da Silva, N.L.S. da Fonseca, R. Boutaba, Evaluation of the employment of UAVs as fog nodes, IEEE Wirel. Commun. 28 (5) (2021) 20–27, https://doi.org/10.1109/MWC.101.2100018.

[35] J. Wang, K. Liu, J. Pan, Online UAV-mounted edge server dispatching for mobile-to-mobile edge computing, IEEE Int. Things J. 7 (2) (2020) 1375–1386, https://doi.org/10.1109/JIOT.2019.2954798.

[36] S. Jeong, O. Simeone, J. Kang, Mobile edge computing via a UAV-mounted cloudlet: optimization of bit allocation and path planning, IEEE Trans. Veh. Technol. 67 (3) (2018) 2049–2063, https://doi.org/10.1109/TVT.2017.2706308.

[37] J. Ji, K. Zhu, et al., Energy consumption minimization in UAV-assisted mobile-edge computing systems: joint resource allocation and trajectory design, IEEE Int. Things J. 8 (10) (2021) 8570–8584, https://doi.org/10.1109/JIOT.2020.3046788.

[38] M. Li, N. Cheng, et al., Energy-efficient UAV-assisted mobile edge computing: resource allocation and trajectory optimization, IEEE Trans. Veh. Technol. 69 (3) (2020) 3424–3438, https://doi.org/10.1109/TVT.2020.2968343.
[39] M. Zhao, W. Li, et al., Fairness-aware task scheduling and resource allocation in UAV-enabled mobile edge computing networks, IEEE Trans. Green Commun. Netw. 5 (4) (2021) 2174–2187, https://doi.org/10.1109/TGCN.2021.3095070.
[40] K. Gray, T.D. Nadeau, Network Function Virtualization, 1st edition, Elsevier Inc., Cambridge, MA, USA, 2016.
[41] C. Grasso, R. Raftopoulos, G. Schembra, Slicing a FANET for heterogeneous delay-constrained applications, Comput. Commun. 195 (2022) 362–375, https://doi.org/10.1016/j.comcom.2022.08.024.
[42] J. Lyu, Y. Zeng, R. Zhang, Uav-aided offloading for cellular hotspot, IEEE Trans. Wirel. Commun. 17 (6) (2018) 3988–4001, https://doi.org/10.1109/TWC.2018.2818734.
[43] M.M. Azari, F. Rosas, et al., Ultra reliable UAV communication using altitude and cooperation diversity, IEEE Trans. Commun. 66 (1) (2018) 330–344, https://doi.org/10.1109/TCOMM.2017.2746105.
[44] A. Fasano, G. Di Blasio, et al., Optimal discrete bit loading for DMT based constrained multicarrier systems, in: Proceeding of IEEE Int. Symp. Inf. Theory, ISIT'02, IEEE, Lausanne, Switzerland, 2002, p. 243.
[45] E. Baccarelli, R. Cusaniand, S. Galli, A novel adaptive receiver with enhanced channel tracking capability for TDMA-based mobile radio communications, IEEE J. Sel. Areas Commun. 16 (9) (1998) 1630–1639, https://doi.org/10.1109/49.737632.
[46] E. Baccarelli, M. Biagi, et al., Broadband Wireless Access Networks: a Roadmap on Emerging Trends and Standards, John Wiley & Sons, Ltd, 2005, pp. 215–240, Ch. 14.
[47] M.S. Bazaraa, H.D. Sherali, C.M. Shetty, Nonlinear Programming: Theory and Algorithms, 3rd edition, Wiley-Interscience, Hoboken, NJ, USA, 2006.
[48] W. Stallings, 5G Wireless: a Comprehensive Introduction, 1st edition, Addison-Wesley Professional, Pearson, 2021.
[49] E.T. Michailidis, N. Nomikos, et al., Three-dimensional modeling of mmWave doubly massive MIMO aerial fading channels, IEEE Trans. Veh. Technol. 69 (2) (2020 February), https://doi.org/10.1109/TVT.2019.2956460.
[50] E. Baccarelli, M. Biagi, C. Pelizzoni, On the information throughput and optimized power allocation for MIMO wireless systems with imperfect channel estimation, IEEE Trans. Signal Process. 53 (7) (2005) 2335–2347, https://doi.org/10.1109/TSP.2005.849165.
[51] E. Baccarelli, M. Biagi, Power-allocation policy and optimized design of multiple-antenna systems with imperfect channel estimation, IEEE Trans. Veh. Technol. 53 (1) (2004) 136–145, https://doi.org/10.1109/TVT.2003.822025.
[52] E. Baccarelli, M. Biagi, et al., Optimized power allocation for multiantenna systems impaired by multiple access interference and imperfect channel estimation, IEEE Trans. Veh. Technol. 56 (5) (2007) 3089–3105, https://doi.org/10.1109/TVT.2007.900514.
[53] D. Amendola, N. Cordeschi, E. Baccarelli, Bandwidth management VMs live migration in wireless Fog Computing for 5G networks, in: Proceeding of 5th IEEE Int. Conf. Cloud Netw., Cloudnet'16, IEEE, Pisa, Italy, 2016, pp. 21–26.
[54] H. Mei, K. Yang, et al., Joint trajectory-resource optimization in UAV-enabled edge-cloud system with virtualized mobile clone, IEEE Int. Things J. 7 (7) (2020) 5906–5921, https://doi.org/10.1109/JIOT.2019.2952677.
[55] N. Sharma, M. Magarini, et al., On-demand ultra-dense cloud drone networks: opportunities, challenges and benefits, IEEE Commun. Mag. 56 (8) (2018) 85–91, https://doi.org/10.1109/MCOM.2018.1701001.